SEMI-EMPIRICAL EQUATION FOR THE SYMMETRIC HYDROSTATIC COLLAPSE OF FLEXIBLE PIPES

Matheus Costa dos Santos

Dissertação de Mestrado apresentada ao Programa de Pós-graduação em Engenharia Civil, COPPE, da Universidade Federal do Rio de Janeiro, como parte dos requisitos necessários à obtenção do título de Mestre em Engenharia Civil.

Orientador:
José Renato Mendes de Sousa, D.Sc.

Rio de Janeiro

Setembro de 2024

SEMI-EMPIRICAL EQUATION FOR THE SYMMETRIC HYDROSTATIC COLLAPSE OF FLEXIBLE PIPES

Matheus Costa dos Santos

DISSERTAÇÃO SUBMETIDA AO CORPO DOCENTE DO INSTITUTO ALBERTO LUIZ COIMBRA DE PÓS-GRADUAÇÃO E PESQUISA DE ENGENHARIA DA UNIVERSIDADE FEDERAL DO RIO DE JANEIRO COMO PARTE DOS REQUISITOS NECESSÁRIOS PARA A OBTENÇÃO DO GRAU DE MESTRE EM CIÊNCIAS EM ENGENHARIA CIVIL.

Orientador: Prof. José Renato Mendes de Sousa, D.Sc.

Aprovada por: Prof. José Renato Mendes de Sousa, D.Sc.

Prof. Luis Volnei Sudati Sagrilo, D.Sc.

Prof. Murilo Augusto Vaz, PhD.

Dr. George Carneiro Campello, D.Sc.

RIO DE JANEIRO, RJ – BRASIL

SETEMBRO DE 2024

Santos, Matheus Costa dos.

Semi-Empirical Equation for the Symmetric Hydrostatic Collapse of Flexible Pipes / Matheus Costa dos Santos – Rio de Janeiro: UFRJ / COPPE, 2024.

VI, 67 p.: il.; 29,7 cm

Advisor: José Renato Mendes de Sousa

Dissertação (Mestrado) – UFRJ / COPPE / Programa de Engenharia Civil, 2024.

References: p. 63-66.

1. Introduction. 2. Bibliographic Research. 3. Numerical Model for Hydrostatic Collapse. 4. Semi-Empirical Formulation 5. Discussion. 6. Conclusions. I. de Sousa, José Renato Mendes. II. Universidade Federal do Rio de Janeiro, COPPE, Programa de Engenharia Civil. III. Título.

Resumo da Dissertação apresentada à COPPE/ UFRJ como parte dos requisitos necessários para a obtenção do grau de Mestre em Ciências (M.Sc.)

EQUAÇÃO SEMIEMPÍRICA PARA O COLAPSO HIDROSTÁTICO SIMÉTRICO DE DUTOS FLEXÍVEIS

Matheus Costa dos Santos

Setembro/2024

Orientador: José Renato Mendes de Sousa

Programa: Engenharia Civil

Nesta dissertação de mestrado, o colapso hidrostático simétrico (em forma de "coração") da carcaça intertravada de dutos flexíveis é estudado. Inicialmente, propõe-se um modelo numérico, baseado no Método dos Elementos Finitos (MEF), para predição desse tipo de falha. O modelo considera apenas as camadas resistentes a cargas radiais, isto é, a carcaça intertravada, a camada plástica interna e a armadura de pressão, representando-as através de elementos de casca equivalentes. A interação entre as camadas é garantida por meio de elementos de contato. Utilizando as pressões de colapso calculadas por esse modelo e avaliando os principais parâmetros envolvidos na resposta, um banco de dados será construído e, posteriormente, processado através de um programa de regressão simbólica (RS). O resultado dessa análise é uma expressão para cálculo da pressão de colapso. Os resultados dessa expressão são comparados aos obtidos em análises numéricas. Uma discussão sobre a ocorrência do modo simétrico em detrimento ao bissimétrico também será apresentada.

Abstract of Dissertation presented to COPPE/ UFRJ as partial fulfillment of the requirements for the degree of Master of Science (M.Sc.)

SEMI-EMPIRICAL EQUATION FOR THE SYMMETRIC HYDROSTATIC COLLAPSE OF FLEXIBLE PIPES

Matheus Costa dos Santos

September/2024

Advisor: José Renato Mendes de Sousa

Department: Civil Engineering

This master's dissertation aims to study the symmetric hydrostatic collapse of flexible pipes' interlocked carcass. First, a numerical model based on the Finite Element (FE) method is proposed to predict this failure mode. The model considers only the layers that resist radial loading: the interlocked carcass, the polymeric inner sheath, and the pressure armor, represented through equivalent shell elements. The interaction between layers is achieved using contact elements. A database is constructed, exploring the key parameters involved in the response of this failure mode and their correspondent collapse pressures, acquired by the numerical model. Afterward, a symbolic regression (SR) analysis was used to process these results. The outcome of the SR analysis is an analytical equation to calculate the symmetric collapse pressure of flexible pipes. Finally, the results of the analytical equation are compared with the numerical results. A discussion about the occurrence of the symmetric mode of failure instead of the bisymmetric mode of failure is presented.

TABLE OF CONTENTS

1. INTRODUCTION 1

    1.1 Background and Motivation 1
    1.2 Dissertation Goal 6
    1.3 Dissertation Organization 7

2. BIBLIOGRAPHIC RESEARCH 8

    2.1 Bisymmetric Collapse 8
    2.2 Symmetric Collapse 12

3. NUMERICAL MODEL FOR HYDROSTATIC COLLAPSE 17

    3.1 Layers Modeling 18
    3.2 Material Nonlinearities 22
    3.3 Contact Nonlinearities 23
    3.4 Geometric Imperfections 24
    3.5 Boundary Conditions and Loads 25
    3.6 Model Implementation 26
    3.7 Case Study 29
        3.7.1 Bisymmetric Collapse 30
        3.7.2 Symmetric Collapse 35

4. SEMI-EMPIRICAL FORMULATION 43

    4.1 Symbolic Regression 43
    4.2 Dimensionless Parameters 44
    4.3 Analytical Equation 47

5. DISCUSSION 54

    5.1 Analytical Equation Evaluation 54
    5.2 Analytical Comparison 56

6. CONCLUSIONS 61

7. REFERENCES 63

APPENDIX A – BISYMMETRIC WET COLLAPSE EQUATIONS 67

LIST OF FIGURES

Figure 1-1: Typical Rough Bore Flexible Pipe (Adapted from API RP 17B, 2014).....1

Figure 1-2: Pressure Armor Cross-Section Profiles (a) Z Profile (b) C Profile (c) T Clip Profile (d) T Profile (e) PSI Profile (MIYAZAKI, 2016).....2

Figure 1-3: Interlocked Carcass Cross-Section (API RP 17B, 2014).....3

Figure 1-4: Subsea Layout (Adapted from ©TechnipFMC plc, 2019).....4

Figure 1-5: Collapse Failure Modes: (a) Bisymmetric Elliptical (b) Bisymmetric "8" (c) Symmetric (Adapted from SOUSA *et al.* 2018).....5

Figure 2-1: Initial Dent in a Flexible Pipe Subjected to External Pressure.....14

Figure 3-1: Finite Element Model View – a) Left b) Front c) Isometric.....17

Figure 3-2: Tendon Axis Coordinates (SOUSA *et al.,* 2018).....20

Figure 3-3: Schematic Stress vs Strain Curve (SOUSA *et al.,* 2022).....22

Figure 3-4: Ovalization of a Layer.....24

Figure 3-5: Load Unbalance with Bisymmetrical Imperfection – a)Front View b) Oblique View.....26

Figure 3-6: Finite Element Mesh (SOUSA *et al.* 2018).....27

Figure 3-7: Pressure vs Ovalization Curve for $\boldsymbol{o = 0.1\%, \sigma efc = \sigma efp = 200\ MPa}$ – Bisymmetric Collapse.....30

Figure 3-8: Nodal Displacements (mm) at Collapse Pressure – Bisymmetric Collapse 31

Figure 3-9: Nodal Displacements (mm) at Analysis End – Bisymmetric Collapse.....31

Figure 3-10: Stress Distribution (MPa) at Collapse Pressure – Bisymmetric Collapse .32

Figure 3-11: Stress Distribution at Analysis End – Bisymmetric Collapse.....32

Figure 3-12: Stress Ratio – Load Progression.....33

Figure 3-13: Stress Ratio – Collapse Pressure.....34

Figure 3-14: Pressure vs Ovalization Curve for $\boldsymbol{o = 0.1\%, \sigma efc = \sigma efp = 200\ MPa}$ – Symmetric Collapse.....35

Figure 3-15: Nodal Displacements (mm) at Collapse Pressure – Symmetric Collapse .36

Figure 3-16: Nodal Displacements (mm) at Analysis End – Symmetric Collapse.....36

Figure 3-17: Stress Ratio – Symmetric Collapse.....37

Figure 3-18: Stress Ratio – Symmetric Collapse.....38

Figure 3-19: Bissymetric vs Symmetric Stress Ratio @ Collapse Pressure.....38

Figure 3-20: Symmetric Collapse Pressure vs Ovalization - $\boldsymbol{\sigma efp = 200MPa}$.....39
Figure 3-21: Symmetric Collapse Pressure vs Ovalization - $\boldsymbol{\sigma efp = 400MPa}$.....40
Figure 3-22: Symmetric Collapse Pressure vs Ovalization - $\boldsymbol{\sigma efp = 600MPa}$.....40
Figure 3-23: Symmetric Collapse Pressure vs Ovalization - $\boldsymbol{\sigma efp = 800MPa}$.....41
Figure 3-24: Symmetric Collapse Pressure vs Ovalization - $\boldsymbol{\sigma efp = 900MPa}$.....41
Figure 4-1: Dimensionless Parameters S1 and ST Analysis.....49
Figure 4-2: Dimensionless Parameters S2 Analysis.....50
Figure 4-3: Predicted Dimensionless Symmetric Collapse Pressure.....50
Figure 4-4: Prediction Residue Histogram.....52
Figure 4-5: Prediction Percentual Residue Histogram.....52
Figure 4-6: Percentual Residue Distribution vs Symmetric Collapse Pressure.....53
Figure 5-1: Predicted Dimensionless Symmetric Collapse Pressure – Structure 1 and 2 55
Figure 5-2: Bisymmetric vs Symmetric Wet Collapse Pressure.....56
Figure 5-3: Bisymmetric ≤ Symmetric Wet Collapse Pressure.....57
Figure 5-4: Collapse Pressure vs Dimensionless Parameters.....58
Figure 5-5: Collapse Pressure vs **Πr**.....59
Figure 5-6: Dimensionless Parameters Histogram.....60

CHAPTER 1
INTRODUCTION

1.1 Background and Motivation

The IFP (Institut Français du Pétrol / French Institute of Petroleum) conceived the initial flexible pipes in the 1960s. Today, the API RP 17B (2014) divides the flexible pipes into two main groups: bonded flexible pipes in which the the metallic components are attached in an elastomeric vulcanized matrix guarantees a coupled behavior of all pipe's layers; and unbonded or non-bonded flexible pipes, where the multiple layers have free relative movement, with independence between metallic and polymeric layers. This dissertation focuses on unbonded flexible pipes, which will be named simply flexible pipes.

The offshore oil and gas industry has used unbonded flexible pipes since the 1970s. More specifically, applying these structures to transport oil and gas in Brazil poses important technological challenges once the exploration water depths have increased, reaching depths from 2,500 meters to 3,000 meters, e.g., in Brazilian pre-salt basins (TechnipFMC plc, 2019).

Composed of a superposition of metallic and polymeric layers, one advantage of flexible pipes is the complacency with floating offshore facilities due to their combined high axial strength and low bending stiffness compared to conventional rigid pipes. Figure 1-1 schematically shows the main layers in a typical unbonded rough bore flexible pipe.

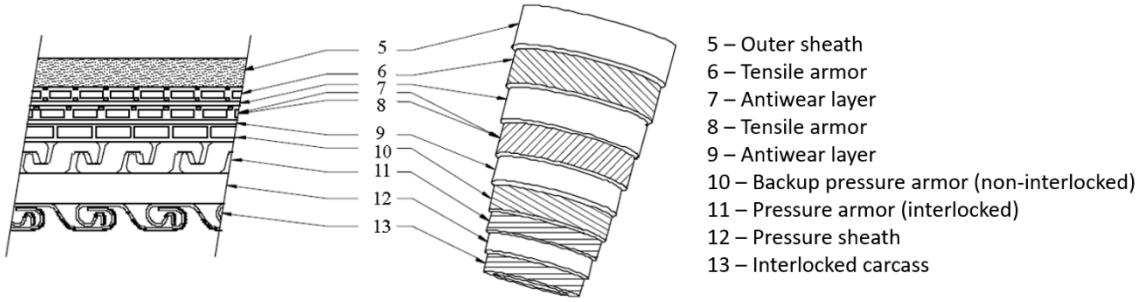

Figure 1-1: Typical Rough Bore Flexible Pipe (Adapted from API RP 17B, 2014)

In Figure 1-1, the polymeric layers guarantee tightness and/or reduce the friction and wear between layers. On the other hand, the metallic components (tensile armors, pressure armor, and interlocked carcass) provide the flexible pipe's structural strength. The tensile armors comprise several approximately rectangular cross-sectional steel wires helically laid in two or four layers, cross-wound at angles between 20º and 55º. These layers are mainly responsible for resisting axial loading but may also contribute to pressure loading resistance (API RP 17B, 2014). Moreover, the pressure armor is usually made from one or two Z-shaped steel wires (other cross-sections are possible, as seen in Figure 1-2) wound at angles close to 90º with the primary function of supporting the system's internal pressure, also contributing to external pressure and radial crushing resistance. Finally, the carcass is made from profiled steel strips (Figure 1-3) helically wound around the flexible pipe longitudinal axis and interlocked during its forming process. As this layer is the innermost component of the pipe, its construction is performed over a mandrel, guaranteeing a high precision on the diameter tolerances, thus leading to a small ovalization, around 0.2%, according to the API RP 17B (2014).

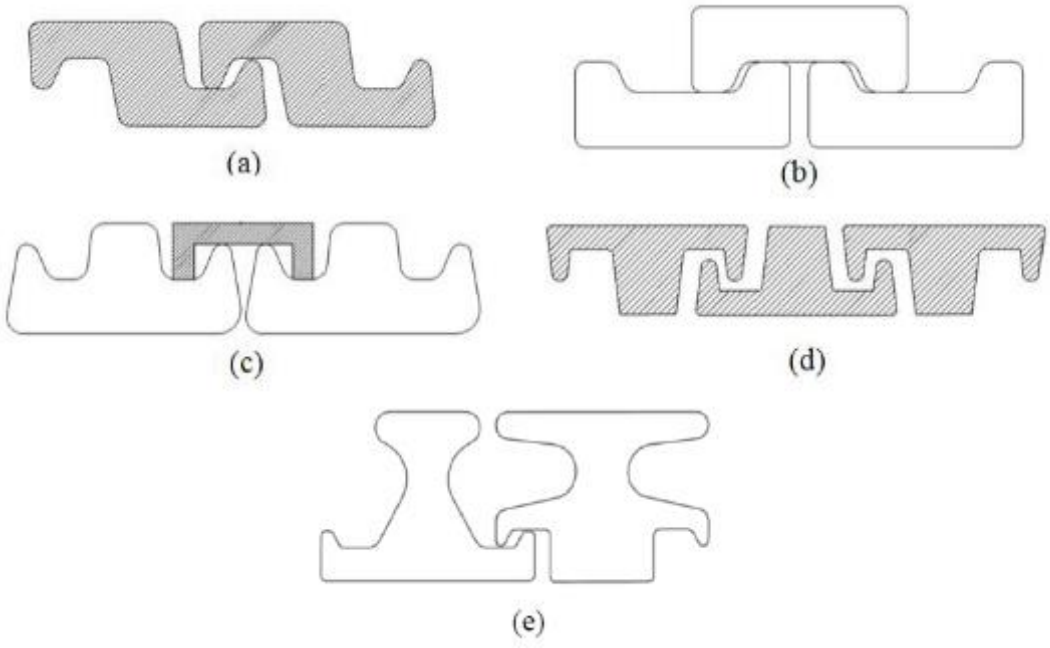

Figure 1-2: Pressure Armor Cross-Section Profiles (a) Z Profile (b) C Profile (c) T Clip Profile (d) T Profile (e) PSI Profile (MIYAZAKI, 2016)

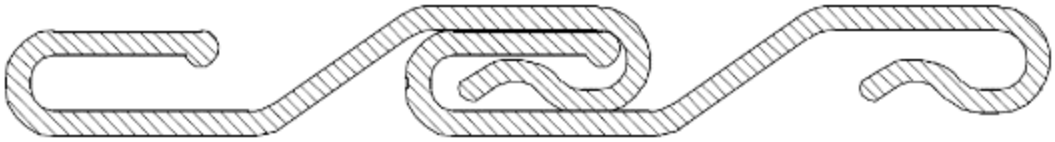

Figure 1-3: Interlocked Carcass Cross-Section (API RP 17B, 2014)

According to the API RP 17B (2014), unbonded flexible pipes are subdivided into three families. The first family (I) is dedicated to smooth-bore flexible structures, which do not contain the interlocked carcass and are used in transporting fluids without gases in their composition. In this structure, the pressure armor is the component that resists both internal and external pressure loading. The second family (II) contains rough bore structures, i.e., flexible pipes with an inner carcass but no pressure armor. Hence, the tensile armors are laid in angles close to 55º to balance the resistance of axial and pressure loads. Finally, the third family (III) is also related to rough bore pipes, but a pressure armor is added to assist the resistance to radial (inward and outward) forces and pressures.

The API SPEC 17J (2014) also classifies flexible pipes according to their application. Risers are flexible pipes, in dynamic or static applications, that connect a platform/buoy/ship to a flowline, seafloor installation, or another platform where the pipe may be freely suspended (free hanging, catenary), restrained to some extent (buoys, chains), totally restrained, or enclosed in a tube (I- or J-tubes). Jumpers are usually short-length flexible pipes connecting two equipment or a floating production unit and a storage floating unit. This application can be subjected to either dynamic or static loads. Finally, the flowlines are defined as flexible pipes with most of their length on the seabed, mainly resisting static loads, such as hydrostatic pressure. Hence, hydrostatic collapse is a critical design failure mode in these structures. A subsea layout representing some of these applications is shown in Figure 1-4.

The collapse of the flexible pipe is characterized by the deformation of its cross-section, restricting, totally or partially, the flow of the fluid in transport (API RP 17B, 2014). The API RP 17B (2014) defines that the evaluation of the flexible pipe collapse strength has to be performed for both the condition of an intact outer polymeric sheath(s) and the condition of a damaged outer polymeric sheath(s), which means to evaluate the flexible pipe collapse pressure on the conditions know as dry annulus condition (or simply

dry collapse) and flooded annulus condition (or simply wet collapse), respectively. The flexible pipe's collapse strength is the minimum pressure between these conditions.

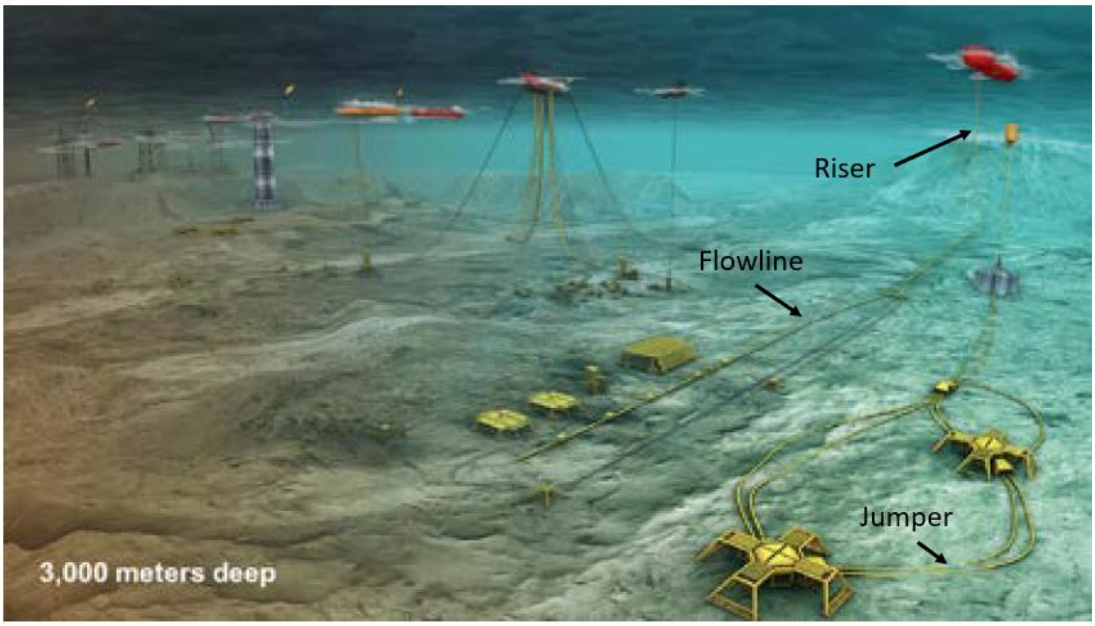

Figure 1-4: Subsea Layout (Adapted from ©TechnipFMC plc, 2019)

In the dry collapse case, the hydrostatic pressure acts over the outermost layer, leading to, possibly, the contribution of all layers to the hydrostatic collapse strength. In general, the contribution of polymeric and tensile armor layers is neglected. On the other hand, the fluid entry on the flexible pipe annulus in wet collapse is through pre-existing or operational damages in the outer polymeric sheath. In this way, the hydrostatic pressure acts directly over the innermost sealed polymeric layer, which is usually the internal pressure sheath. In this condition, only the interlocked carcass, aided by the pressure armor, resists the hydrostatic loading.

Both the flexible pipe type (smooth bore or rough bore) and the annulus conditions influence the hydrostatic collapse mode of the structure. Figure 1-5 presents the hydrostatic collapse failure modes usually observed in flexible pipes.

Figure 1-5: Collapse Failure Modes: (a) Bisymmetric Elliptical (b) Bisymmetric "8" (c) Symmetric (Adapted from SOUSA *et al.* 2018)

Figure 1-5 (a) shows the elliptical or ovalization failure mode related to smooth-bore flexible pipes from family I or the wet/dry collapse of rough-bore pipes from family II. The failure modes shown in Figure 1-5 (b) and (c) are commonly named "eight-shaped" and "heart-shaped" modes, respectively. The "eight-shaped" can occur in dry or flooded condition in rough bore flexible pipes of family III. In dry conditions, both the pressure armor and carcass fail, while in the flooded conditions only the carcass reaches failure, confined within the pressure armor. The "heart-shaped" failure mode is restricted to the flooded annulus condition in rough bore flexible pipes of family III and is also defined by the failure of the carcass confined by the pressure armor. In this dissertation, for simplicity, the elliptical and the "eight-shaped" failure modes are called bisymmetric modes, while the "heart-shaped" mode is named symmetric.

Some paths can be explored to evaluate the collapse strength of a flexible structure for both dry and wet conditions. Experimental tests would be the "gold standard" for assessing the collapse resistance of flexible pipes, but the execution of an experiment demands high costs and specialized equipment. Therefore, a small, limited number of experimental results are available in the literature (SILVA, 2014 and SOUZA, 2002).

Alternatively, whether based on numerical or analytical modeling, theoretical models have substantially lower costs than experimental tests. However, these models have to deal with some difficulties related to the modeling of (SOUSA *et al.*, 2018; and LI *et al.*, 2018): the inner carcass and the pressure armor complex cross-sections; interlayer and intralayer contact interactions; material nonlinearities; manufacturing

and/or operational-induced imperfections, such as ovalities, interlayer gaps, and residual stresses in the resisting layers; and bending effects.

Hence, the prediction of the collapse pressure of a flexible pipe is not trivial, as it is a highly nonlinear phenomenon that may induce different failure modes depending on the layers' characteristics and imperfections, as well as the pipe's operational conditions. Moreover, most of these models require a significant computational effort to calculate the collapse loads, which is undesirable, particularly in the early design phases of a flexible pipe. Notably, while several studies have been devoted to studying the bisymmetric failure mode, the literature has not adequately addressed the prediction of the symmetric failure mode. This dissertation thus focuses on studying the symmetric collapse failure mode in flexible pipes.

1.2 Dissertation Goal

This dissertation's initial goal is to propose an FE model reproducing the symmetric collapse mode, taking advantage of the propositions presented by PROTASIO (2017) and SOUSA *et al.* (2022), where the bisymmetric collapse mode was investigated.

This model was then employed to analyze a set of flexible pipes representing structures in operation worldwide, and the obtained results formed a database that correlates the structures' characteristics and the respective collapse pressures. After that, the second goal of this dissertation was achieved, i.e., a symbolic regression (SR) software was used to obtain a semi-empirical expression to calculate the symmetric hydrostatic collapse pressure of flexible pipes.

Finally, a study comparing the collapse pressures predicted by the proposed equation and those from the FE model was conducted, accompanied by a discussion on the pipes' preference to collapse following the bisymmetric or the symmetric mode.

1.3 Dissertation Organization

First, Chapter 2 presents a bibliographic review, discussing numerical and analytical models devoted to analyzing the hydrostatic collapse of flexible pipes. This section is divided into studies related to the bisymmetric collapse mode and those associated with the symmetric collapse mode.

Chapter 3 describes the numerical model proposed to simulate the symmetric collapse phenomena. Moreover, Chapter 4 initially presents the procedure for constructing the database employed in the SR analysis, followed by the semi-empirical equation obtention. A discussion regarding the analytical equation's most relevant parameters and the equation's adherence to the database results are also presented.

Chapter 5 discusses the results in two optics. First, the equation obtained in Chapter 4 is evaluated against two new flexible structures that were not part of the database previously. These analyses ensure the equation's robustness to unseen data. Later, a discussion regarding symmetric and bisymmetric failures is presented.

Finally, Chapter 6 presents this dissertation's general conclusions, pointing to future works that may derive from the present work.

CHAPTER 2
BIBLIOGRAPHIC RESEARCH

Numerical and analytical approaches are available in the public literature to study the hydrostatic collapse of flexible pipes. LI *et al.* (2018) divided the numerical models into two groups: the full or complete three-dimensional finite element models and the equivalent finite element models (2D or 3D). Equivalent approaches are also employed in the development of analytical approaches.

In a full three-dimensional finite element model, the true geometry of the carcass and the pressure armor is modeled at its best, thus assuming few geometric, material, and contact simplifications. However, one of its primary drawbacks is the typically high computational cost, linked to the many degrees of freedom required by FE models and potential convergence issues arising from the nonlinearities and boundary conditions involved. These difficulties motivate the development of alternative approaches, such as the equivalent layer approach.

In an equivalent layer model, the intricate layer structure of the carcass and pressure armor is simplified by representing them as equivalent cylinders or rings that possess the same mechanical properties as the actual layers. Using orthotropic material properties with an equivalent thickness guarantees an adequate representation of the axial and bending stiffness of the tendon. Additionally, interlayer contact and geometric nonlinearities can be effectively managed because the mechanical properties of the equivalent layers match those of the real carcass and pressure layers.

In the following sections, the use of these approaches to predict the bisymmetric and symmetric collapse failure modes is discussed, enlightened by the studies published in the public literature.

2.1 Bisymmetric Collapse

Regarding predicting the hydrostatic pressure necessary to initialize the bisymmetric collapse of ovalized pipes, the analytical equation proposed by TIMOSHENKO & GERE (1961) is the starting point. FERGESTAD & LØTVEIT (2017) present Eq. (1), based on the TIMOSHENKO & GERE (1961) equation, to evaluate the

collapse pressure of flexible pipes. The collapse pressure p is define as the smallest root of Eq. (1).

$$p^2 - \left[\frac{F_f t \cdot \sigma_{ef}}{r} + p_{el}\left(1 + \frac{Et^2 \cdot F_f \cdot r \cdot o}{2EI_{eq}}\right)\right]p + \frac{p_{el} \cdot \sigma_{ef} \cdot F_f t}{r} = 0 \quad \textbf{(1)}$$

where t is the layer thickness, r the mean radius, and F_f the fill factor (Eq. (2)); E is the layer material Young modulus and EI_{eq} is the equivalent bending stiffness (Eq. (3)), as defined by FERGESTAD & LØTVEIT (2017). The elastic collapse pressure is given by Eq. (4).

$$F_f = \frac{n \cdot A}{\mathrm{L_p} \cdot t} \quad \textbf{(2)}$$

$$EI_{eq} = K \cdot n \cdot \frac{E \cdot I'_y}{L_p} \quad \textbf{(3)}$$

$$p_{el} = \frac{3 \cdot EI_{eq}}{r^3} \quad \textbf{(4)}$$

where I'_y is the smallest principal moment of inertia of the tendon's cross-section with cross-secion area A, n is the number of tendons that compose the layer, and L_p is the layer pitch. Further development of these equations is presented in Section 3.1.

API RP 17B (2014) defines the ovalization o following Eq. (5):

$$o = \frac{D_{max} - D_{mín}}{D_{max} + D_{mín}} \quad \textbf{(5)}$$

where $D_{mín}$ and D_{max} are the minimum and maximum diameter, respectively, of the flexible pipe.

As per FERGESTAD & LØTVEIT (2017) definition, the collapse occurs when the stress at the outermost fiber of the carcass reaches the material yield strength. In that way, assuming that there is a residual σ_r in the outermost fiber, the yield strength σ_f is reduced to an effective stress σ_{ef} given by:

$$\sigma_{ef} = \sigma_f - \sigma_r \tag{6}$$

The estimate of the residual stress σ_r can be made assuming a total cross-section plastification, subjected to a constant stress σ_u during the manufacturing and that the elastic unloading occurs with zero moment. Hence:

$$\sigma_r = \frac{\sigma_u W_p}{W_e} - \sigma_u \tag{7}$$

where W_p e W_e are the plastic area moment and the elastic area moment, respectively.

SOUSA *et al.* (2018) highlight that the use of σ_u equivalent to the material ultimate tensile stress is conservative when observing some predictions regarding residual stress distribution along the cross-section of pressure armors. Therefore, SOUSA *et al.* (2018) suggest to correlate the σ_u with the induced deformation of the cross-section outermost fiber during the tendons laying process ε_u, indicated by SAEVIK *et al.* (2001), and given by Eq. (8):

$$\varepsilon_u = \frac{t}{2r} \cdot \frac{1}{sin^2(\alpha)} \tag{8}$$

where α is the laying angle of the layer of interest.

However, Eq. (1) can only be applied to the collapse of family I and II pipes or the dry collapse of family III pipes, i.e., the wet collapse pressure cannot be estimated. Moreover, the equation is only valid for small geometric imperfections *o*.

PAUMIER *et al.* (2009) calibrated the equation proposed by TIMOSHENKO & GERE (1961), relying on FE analyses and an extensive database of experimental tests. The obtained analytical model considers the different layers' material nonlinearity and the pipe's ovalization. Moreover, the model was certified by a third party for both straight and curved pipes. PAUMIER *et al.* (2009) show that the curved condition can significantly influence the collapse strength of the pipe once the introduction of a bending load unbalances the equilibrium of the system's loads.

NETO *et al.* (2012) developed a full three-dimensional FE model, considering the detailed geometries of the interlocked carcass and the pressure armor. The model also contains inner and outer polymeric sheaths. The study initially explored the influence of the length of the numerical model, showing that 30 pitches of the inner carcass provided stable results (free from boundary conditions effects) in all cases. Moreover, it was shown that the structure "chooses" the collapse mode that requires less energy, depending on the conditions to which it is subjected to, such as the type of initial imperfection and the relation between the stiffness of the resistant pipe layers (inner carcass and pressure armor). Also, the influence of the curvature imposed on the flexible pipe was once again a subject of discussion, given its contribution to reducing the flexible pipe collapse strength.

SILVA (2014) proposed a simplified FE model based on beam elements. The study also contemplated the execution of two-point static ring tests to indirectly calibrate the stress vs. strain material curves of inner carcasses and pressure armors extracted from 4" and 6" flexible pipes. The calibration process relied on matching the tests' results with those calculated in FE model simulations by numerically modifying the layers' material curves. Then, the FE model was employed to evaluate the collapse strength of the pipes, considering the calibrated curves, and the calculated collapse pressures were compared to the pressures measured in experimental tests conducted in a hyperbaric chamber. The results showed good agreement.

MELENDEZ *et al.* (2017) analyzed the bisymmetric collapse mode of pipes from families II and III using a full three-dimensional FE model. The authors observed

the elliptical shape in the collapsed family II pipe, while the "eight" shape occurred in the family III pipe. Moreover, the eight-shaped mode required more energy (higher collapse pressure) than the elliptical mode due to the restriction imposed by the pressure armor on the carcass displacement.

PROTASIO (2017) and SOUSA *et al.* (2018) proposed a simplified numerical model that uses equivalent orthotropic shell finite elements to predict the bisymmetric collapse pressure of flexible pipes. This model has the advantage of reducing the computational cost of the numerical analysis. Several numerical analyses were conducted considering different pipes, and the obtained results were employed to create a database in which the analyzed pipe characteristics are associated with the respective collapse pressure. The database was then processed through a symbolic regression algorithm to obtain an analytical equation to calculate the critical collapse pressure of a given pipe.

This dissertation has the numerical model presented by PROTASIO (2017) and SOUSA et al. (2018) at its baseline, and the symbolic regression approach is also used in the study presented here. The numerical model's boundary and initial conditions were adapted to represent the symmetric collapse phenomena and are detailed in Chapter 3.

2.2 Symmetric Collapse

The symmetric collapse of flexible pipes, as discussed in Section 1.1, is intrinsically linked with wet annulus conditions. The water ingression on the flexible pipe's annulus means the outermost tight polymeric sheath is damaged, and the hydrostatic pressure acts directly over the innermost polymeric sheath. In this way, this type of collapse, like the bisymmetric collapse mode, is confined by the pressure armor, but the deformed shape is different, having a "heart" aspect. The public literature does not clearly state why the carcasses choose one specific collapse mode. Still, as presented in this section, some authors suggest that initial imperfections and bending effects may favor the "heart" collapse mode.

Initially, similar to the bisymmetric collapse mode, the symmetric collapse mode (or "heart-shaped") also has a baseline analytical model, presented initially by GLOCK (1977). Eq. (9) calculates the critical collapse pressure p for a deformable infinite pipe

confined in a stiff pipe without friction between them. Eq (10), on the other hand, considers a confined ring p_r collapse pressure.

$$p = \frac{E}{(1-\nu^2)}\left(\frac{t}{D}\right)^{\frac{11}{5}} \quad \textbf{(9)}$$

$$p_r = E\left(\frac{t}{D}\right)^{\frac{11}{5}} \quad \textbf{(10)}$$

where t is the thickness of the cylinder or ring, and D represents the mean diameter of the circular section; E and ν are the material Young modulus and Poisson coefficient, respectively.

Once again, PAUMIER *et al.* (2009) extended the application of GLOCK's (1977) equations by calibrating them against experimental data. The equation was also certified by a third party but was not presented in the study.

NETO *et al.* (2012) also studied the influence of the curvature on the occurrence of both symmetric and bisymmetric collapse modes. The authors showed that the bending load in a wet collapse analysis induced the symmetric collapse mode, even though the initial imperfection was bisymmetric. According to the authors, the failure occurred because the curvature acted as an imperfection in just one plane of symmetry, favoring the symmetric shape. Moreover, NETO *et al.* (2012) indicated that different pressure armors induced different collapse modes for the same interlocked carcass. In the case of a very stiff pressure armor, in comparison to the stiffness of the carcass, the symmetric collapse mode was favored, even considering a bisymmetric imperfection.

ALEXELSSON & SKJERVE (2014) proposed three-dimensional and two-dimensional FE models to study the influence of an initial axial pre-load applied to the carcass, the effects of curvature on the flexible pipe, the layers' ovalization, the gaps between adjacent layers, and the pressure increment velocity on the collapse pressure of flexible pipes. The main conclusions were:

- Axial pre-loading and bending loads reduce the flexible pipe collapse strength;
- Two-dimensional FE models can generate accurate results if the analysis does not present axial and bending loads.
- Possible interlayer gaps were considered the most important geometrical parameter;
- The pressure increment rate influences the collapse pressure of numerical finite element models;

BAI *et al.* (2016) studied the confined collapse using a simplified FE model of two concentric cylinders. An initial imperfection was introduced in the model to induce the structure's instability following the symmetric collapse mode. This imperfection is imposed by radially deforming the structure, allowing its elastic return and leaving residual radial displacements, as shown in Figure 2-1. The work suggests a parametric study to determine the value of δ_0 that suits the collapse model.

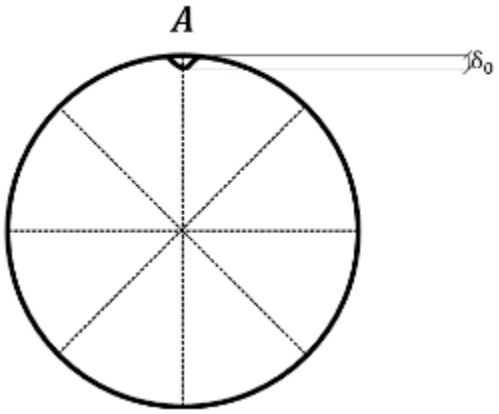

Figure 2-1: Initial Dent in a Flexible Pipe Subjected to External Pressure

BAI *et al.* (2016) also explored the effect of different ratios ϕ_k, Eq. (11), i.e., the ratio between the bending stiffness of the outermost and innermost layers and $\phi_D = D/t$.

$$\phi_k = \frac{E_0}{E_i}\frac{t_{eq_o}^3}{t_{eq_i}^3}\frac{R_{eq_i}^3}{R_{eq_o}^3} \quad \textbf{(11)}$$

where subscript i represents the properties of the innermost layer and subscript o the properties of the outermost layer, t_{eq} and I_{eq} are the equivalent thickness and equivalent moment of inertia, Eq. (12), R_{eq} is the mean radius and E the modulus of elasticity of the layer's material.

$$t_{eq} = \sqrt[3]{12\, I_{eq}} \quad \textbf{(12)}$$

BAI *et al.* (2016) demonstrated that the critical collapse pressure increases with the increment of ϕ_k. In the particular case of $\phi_k < 1$, the problem can be simplified as the collapse analysis of the inner cylinder supported by two springs and for $\phi_k > 60$, the GLOCK's (1977) model can be used (Eq. (9) and (10)). Finally, BAI *et al.* (2016) suggest that for better comprehension of the collapse phenomena, the elastic-plastic behavior of the innermost layer must be considered, also considering the initial geometrical imperfection and the friction between surfaces in direct contact.

Regarding wet collapse analysis, LI *et al.* (2020) highlight that the collapse failure shape is intrinsically linked with the initial imperfection imposed. Then, inserting a symmetric imperfection leads to the occurrence of the symmetric or "heart-shaped" form, and a bisymmetric initial imperfection induces the bisymmetric shape of the collapse. Moreover, LI et al. (2020) also present a two-dimensional equivalent half-section ring model with symmetric boundary conditions. Using this model, the authors highlight that the bisymmetric collapse mode leads to higher collapse pressure than the symmetric mode. In addition, LI et al. (2020) show that the symmetric imperfection could lead to the displacement of the opposite section of the carcass, inducing a "heart-shaped" collapse, either symmetric or bisymmetric. This mechanism is related because the structural failure occurs at a given point, considering the cross-section is not perfectly

symmetric. Once the collapse of the structure occurs, the strain energy will stabilize any other points of possible failure of the carcass immediately.

In general, one could notice the importance of the initial imperfection in symmetric or bisymmetric collapse modes. Moreover, the annulus condition, interlayer gaps and contact between layers, and imposed curvatures tend to induce the symmetric collapse of flexible pipes. These key points are explored in Chapter 3, which presents the proposed numerical model.

CHAPTER 3

NUMERICAL MODEL FOR HYDROSTATIC COLLAPSE

The numerical model used in the present work is based on the model presented by PROTASIO (2017) and SOUSA *et al.* (2018), taking advantage of an equivalent three-dimensional FE model approach. This model represents the interlocked carcass, the inner polymeric layer, and the pressure armor of flexible pipes.

The modeling of those layers is built using an equivalent orthotropic shell approach, which considers geometric and material nonlinearities, as well as contact between layers. SOUSA *et al.* (2018) highlighted that the modifications proposed in their study impact both the hydrostatic collapse analysis time and the effectiveness of these analyses. The model is shown in Figure 3-1.

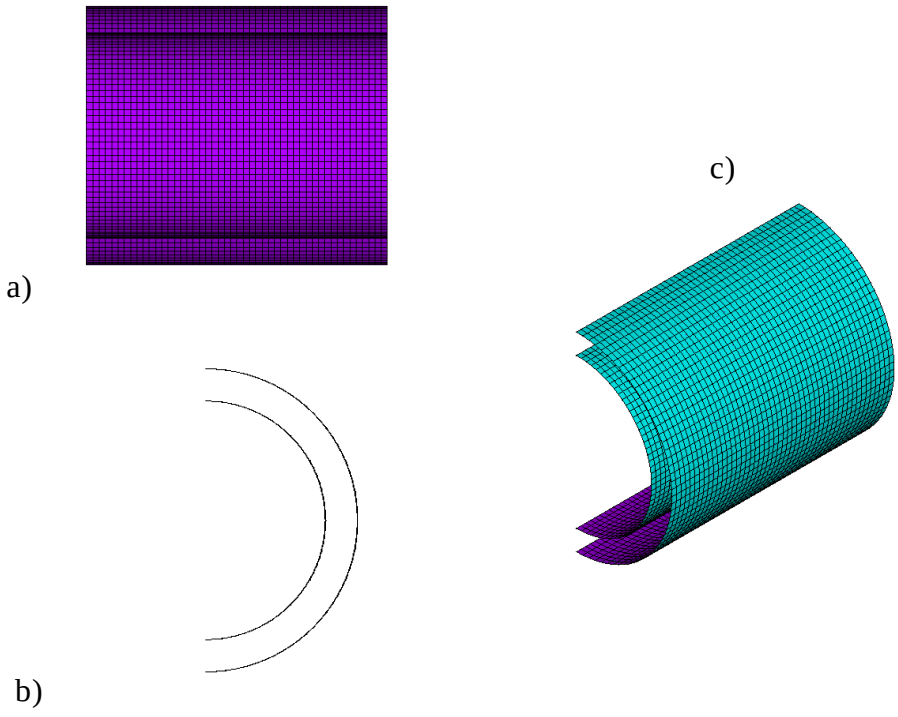

Figure 3-1: Finite Element Model View – a) Left b) Front c) Isometric

3.1 Layers Modeling

The analogy proposed by SOUSA et al. (2018) relies on an equivalence between helical beams and the so-called orthotropic shells to model the interlocked carcass and the pressure armor. This analogy guarantees that the tendon (helical beam) and the shell have the same stiffness, from which equations to calculate the equivalent thickness t_e (Eq. (13)), Young modulus E_e (Eq. (14)) and shear modulus G_e (Eq. (15)) can be calculated.

$$t_e = \sqrt{12 \cdot K \cdot \frac{I'_y}{A}} \tag{13}$$

$$E_e = E\left(\frac{n \cdot A}{L_p \cdot t_e}\right) \tag{14}$$

$$G_e = G\left(\frac{6 \cdot J \cdot n}{L_p \cdot t_e^3}\right) \tag{15}$$

where J is the torsional inertia moment of the tendon, I'_y is the smallest principal moment of inertia of the tendon's cross-section (Eq. (16)) with cross-secion area A, n is the number of tendons that compose the layer, E and G are the material's Young modulus and shear modulus, respectively, and L_p is the layer pitch, given by Eq. (17).

$$I'_y = \frac{I_y + I_z}{2} - \frac{1}{2}\sqrt{(I_z - I_y)^2 + 4 \cdot I_{yz}} \tag{16}$$

where I_y, I_z and I_{yz} are, respectively, the moments of inertia about the y and z axes and the product of inertia of the tendon's cross-section, following the coordinates system of Figure 3-2.

$$L_p = \frac{2\pi r}{tan(\alpha)} \tag{17}$$

where α is the tendon lay angle and r the layer radius.

The factor K depends on the geometrical tendon characteristics and its lay angle. SOUSA *et al.* (2018) proposed an equation to calculate K, based on FE analysis and a symbolic regression model.

$$\begin{aligned} K_j = a_{1,j} + a_{2,j}.\left(\frac{\Pi_{Ij}}{\Pi_{Aj}}\right) + a_{3,j}.(\Pi_{Ij}.\Pi_{\alpha j}) + a_{4,j}.(\Pi_{Aj}.\Pi_{\alpha j}) \\ + \sum_{k=1}^{2}\left\{ a_{k+4,j}.(\Pi_{Ij})^k + a_{k+6,j}.(\Pi_{\alpha j})^k \right. \\ \left. + a_{k+8,j}.\left[\frac{\Pi_{\alpha j}.(\Pi_{Aj})^2}{\Pi_{Ij}}\right]^k + a_{k+10,j}.\left[\frac{\Pi_{\alpha j}.(\Pi_{Ij})^2}{\Pi_{Aj}}\right]^k \right\} \end{aligned} \tag{18}$$

where j=C or P indicates the carcass and pressure armor parameters, respectively. The $a_{ij}, i = 1\ to\ 12$ coefficients depend on the layer and are given in Table 3-1.

Table 3-1: Coefficients $a_{i,j}, i = 1\ to\ 12, j = C\ or\ P$

i	j=C	j=P
1	+1.063661E+00	+6.838550E+01
2	+4.229899E+01	0.000000E+00
3	+2.748450E+03	+8.340695E+02
4	-4.706377E+01	-1.140043E+01
5	-1.000000E+00	-0.742877E+00
6	0.000000E+00	+1.000000E+00
7	0.000000E+00	-0.279188E+00
8	+1.585791E+00	0.000000E+00
9	-0.017376E+00	-3.316204E+01
10	0.000000E+00	+4.097067E+00
11	-1.572021E+05	0.000000E+00
12	0.000000E+00	-5.522764E+10

The dimensionless parameters Π_α, Π_A and Π_I are given by Eq. (19) to (21).

$$\Pi_\alpha = \frac{1}{\alpha} \quad \textbf{(19)}$$

$$\Pi_A = \frac{A}{r.L_p} \quad \textbf{(20)}$$

$$\Pi_I = \frac{I'_y}{r^3.L_p} \quad \textbf{(21)}$$

To correlate the physical properties with the coordinates axis in Figure 3-2, Eqs. (22) and (23) are used. Moreover, based on the hypothesis that the tendon of a layer does not resist loads normal to its laying direction, SOUSA *et al.* (2018) defines $E_{e_y} = 0$ and $\nu_{e_{xy}} = \nu_{e_{yx}} = 0$.

$$G_e = G_{e_{xy}} \quad \textbf{(22)}$$

$$E_e = E_{e_x} \quad \textbf{(23)}$$

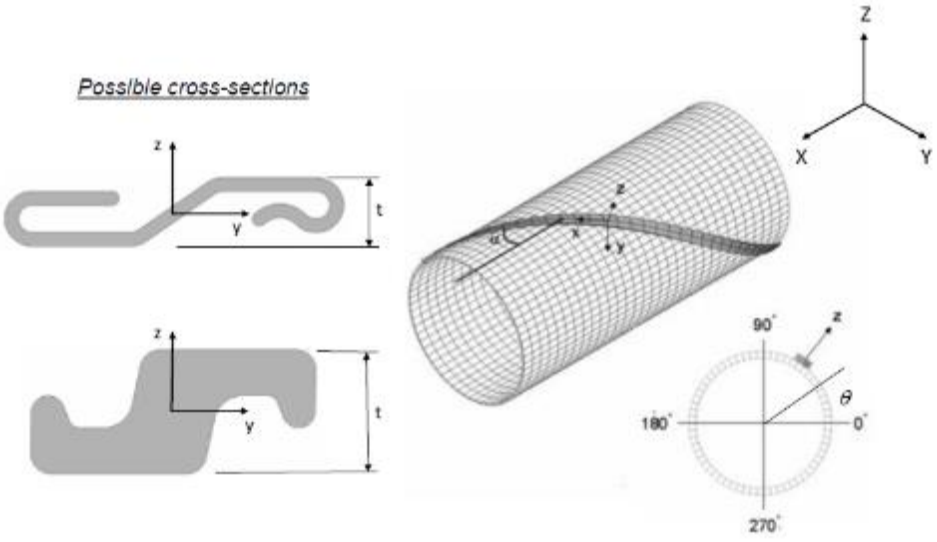

Figure 3-2: Tendon Axis Coordinates (SOUSA *et al.*, 2018)

It is important to notice that the stiffness equivalence does not guarantee the equivalence of the stresses to which the helical tendon and the orthotropic shell are subjected to. To correct this difference, membrane f_m (Eq. (24)), bending f_f (Eq. (25)), and shear f_t (Eq. (26)) factors are proposed.

$$f_m = \frac{L_p \cdot t_e}{n \cdot A} \tag{24}$$

$$f_f = \frac{L_p \cdot t}{n \cdot A} \tag{25}$$

$$f_t = \frac{L_p \cdot t}{n \cdot J} \cdot \frac{t_e^2}{6} \tag{26}$$

Once the stresses are obtained from the equivalent FE model, the stresses on the outermost fibers of the tendons of both the interlocked carcass and the pressure armor are obtained using Eq. (27) and Eq. (28).

$$\sigma_{t_x} = f_m \cdot \sigma_{e_x}^m + f_b \cdot \sigma_{e_x}^b \tag{27}$$

$$\tau_{t_{xy}} = f_t \cdot \tau_{e_{xy}} \tag{28}$$

where σ_{t_x} are $\tau_{t_{xy}}$ the normal stress and the shear stress acting on the tendon cross-section, respectively, and $\sigma_{e_x}^m$, $\sigma_{e_x}^b$ and $\tau_{e_{xy}}$ represent the membrane stress, the bending stress, and the shear stress acting on the orthotropic shell.

Finally, the innermost polymeric sheath is considered a thin isotropic cylinder once this layer is usually extruded on top of the carcass and modeled using an isotropic shell.

3.2 Material Nonlinearities

Once the modeling based on orthotropic shells needs the correction of the stresses, as presented in Section 3.1, to obtain the stresses acting on the tendons of the modeled layers, the direct representation of the nonlinear material behavior is not possible in this type of model (SOUSA *et al.*, 2018). In this way, Eqs. (24) to (28) are implemented in post-processing routines using the ANSYS® commercial software to perform stress corrections.

The interlocked carcass and pressure armor materials are modeled using an equivalent stress vs strain curve, as proposed by SOUSA *et al.* (2022) and shown in Figure 3-3. In such a way, the tangent Young modulus E_t is defined as $10^{-6}\,E$, because ANSYS® does not allow null values. The effective stress σ_{ef} discussed in Section 2.1 is considered in the layers modeling.

Finally, for the polymeric layer, the material behavior was considered linear-elastic.

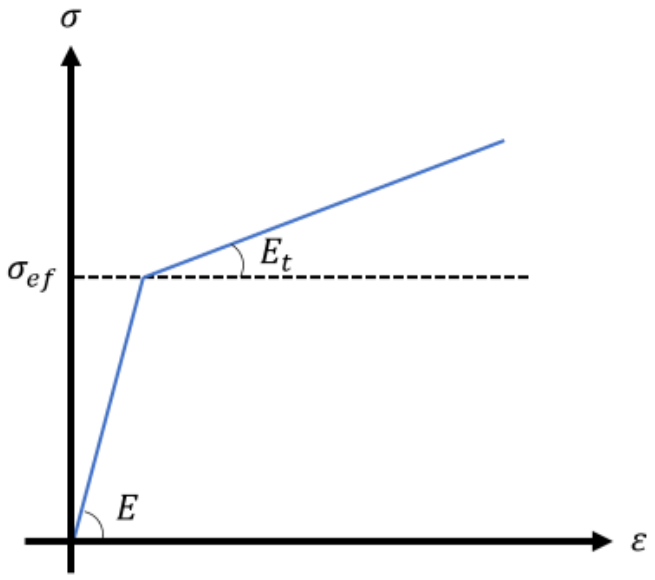

Figure 3-3: Schematic Stress vs Strain Curve (SOUSA *et al.*, 2022)

3.3 Contact Nonlinearities

Based on what was proposed by SOUSA *et al.* (2018), the model used in the present work contains contact elements that allow large displacement between the layers in contact. This analysis is possible by implementing a contact detection algorithm with penalty techniques involved.

In summary, the model must define a value of allowable penetration and normal contact stiffness. In the present case, the maximum allowed penetration value is set to 1% of the thickness of the thinner of the two layers in contact. The normal contact stiffness is given by Eq. (29).

$$K_{n_i} = \frac{\overline{K}_{n_i} \cdot \overline{K}_{n_{i+1}}}{\overline{K}_{n_i} + \overline{K}_{n_{i+1}}}, i = 1,2, \cdots, n_l - 1 \quad \textbf{(29)}$$

where n_l is the number of layers of the flexible pipe and $\overline{K}_{n_i}$ given by:

$$\overline{K}_{n_i} = \frac{E_i}{(1+\nu_i)\cdot(1-2\nu_i)} \cdot \frac{A_{c_i}}{t_i} \quad \textbf{(30)}$$

where ν_i is the Poisson's coefficient of the i_{th} layer material and the contact area A_{c_i} between two layers can be estimated using Eq. (31):

$$A_{c_i} = \frac{2 \cdot \pi \cdot r_{int}}{n_{cd_i}} \cdot \frac{L_t}{n_{ld_i}}, i = 1,2, \cdots, n_l - 1 \quad \textbf{(31)}$$

and r_{int} is the interface radius between layers, n_{cd} and n_{ld} are the number of circumferential and longitudinal divisions of the innermost layer where the contact elements are placed. L_t is the total length of the modeled flexible pipe.

3.4 Geometric Imperfections

As discussed in Chapter 1, one of the difficulties common to collapse analysis models is the consideration of the geometrical imperfections present in a flexible pipe. In this way, the present model accounts for possible gaps between the pressure armor and the polymeric layer. In addition to that, initial imperfections (related to the ovalization) are also taken into consideration.

The gaps are directly modeled by altering the layers' mean radius. Moreover, ovalization is accounted for by considering Eq.(32), where different o values can be assumed for the interlocked carcass and the pressure armor, defining a radial displacement u_0 in the angular position θ of the given cross section considered (Figure 3-4).

$$u_0 = r \cdot o \cdot \cos(2\theta) \quad \textbf{(32)}$$

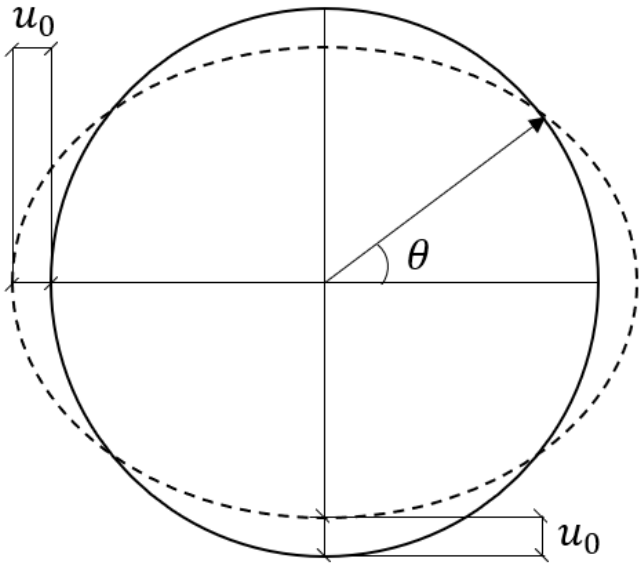

Figure 3-4: Ovalization of a Layer

As discussed in the following topics, these imperfections are directly implemented in the FE mesh build.

3.5 Boundary Conditions and Loads

As this dissertation's goal is the study of the symmetric hydrostatic collapse of flexible pipes, a half-cross-section model with symmetric boundary conditions was constructed.

The nodes in the XZ plane (Figure 3-2) have translations related to the Y axis and rotations regarding the X and Y axes restricted to avoid rigid body motion. Using the coordinates system presented in Figure 3-2, the finite element nodes presented in $\theta = 270°$ and $Z = 0$ have translation in all axis restricted.

Inspired by the curved collapse analysis, where the load unbalance leads to a symmetric hydrostatic collapse mode, this work aims at proposing a load unbalance while applying a bisymmetric ovalization in the FE model, as shown in Figure 3-5, where the variations of the arrows' colors correspond to the pressure loading variation. Eqs. (33) and (34) define the load applied to each node of the numerical model.

$$\Delta_{\mathrm{p}_{ext}} = d_{ip} \cdot p_{ext} \tag{33}$$

$$P_{i+(j-1)\cdot n_{cd\,k}} = p_{ext} + \Delta_{\mathrm{p}_{ext}} \cdot \sin\theta_{ml} \tag{34}$$

where again $i = 1 \ldots n_{cd\,k}$ and $k = 1 \ldots n_{ml}$; p_{ext} is the external pressure applied to the model without the load unbalance. In this way, the load varies from $p_{ext} - \Delta_{\mathrm{p}_{ext}}$, in $\theta_{ml} = 270°$ to $p_{ext} + \Delta_{\mathrm{p}_{ext}}$, in $\theta_{ml} = 90°$, as shown in Figure 3-5. The percentual value d_{ip} was chosen 0.1%, as smaller values did not change the FE model response and yielded convergence issues, increasing the computational cost.

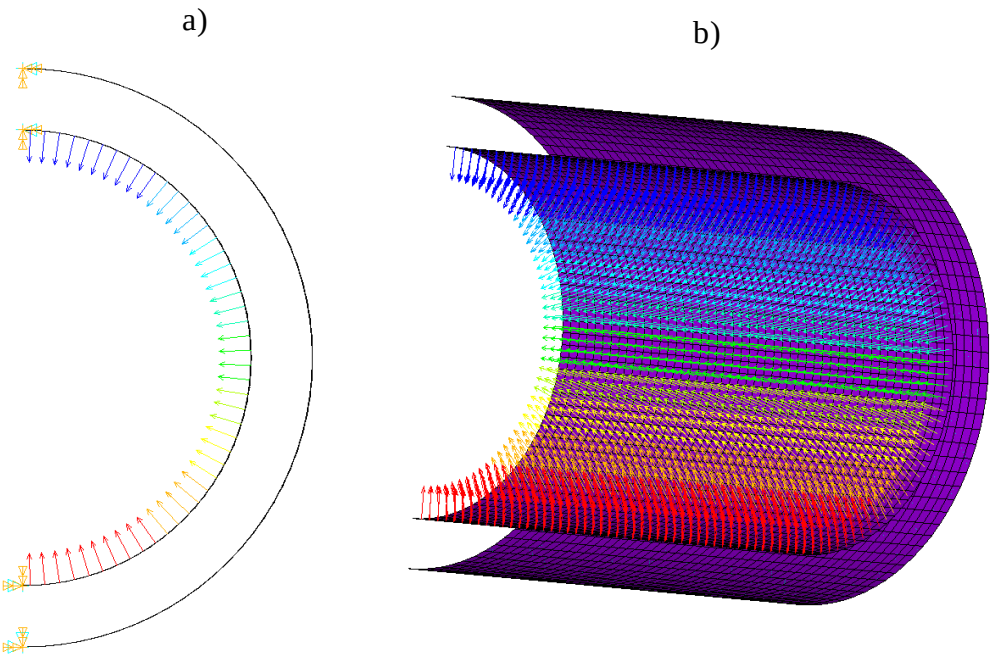

Figure 3-5: Load Unbalance with Bisymmetrical Imperfection – a)Front View b) Oblique View

3.6 Model Implementation

As described in the preceding sections, the numerical model was built using the commercial software ANSYS® with APDL (Ansys Parametric Design Language) macros. All layers are modeled with the nonlinear SHELL181 element, which can represent thin to moderately thick, uniform, or sandwich shells. This element type has six degrees of freedom at each node (translations and rotations in the X, Y, and Z axes). Furthermore, the contact and sliding between layers are simulated with the CONTA174 and TARGE170 elements, placing the former over the polymeric layer (soft layer) and the latter in the metallic armors (rigid layer).

Again, the condition of the polymeric layer being extruded over the carcass leads to the consideration of adherence between this pair of layers, making it possible to model them using layered (sandwich) shell elements, reducing the number of degrees of freedom of the model.

Nevertheless, the position of the polymeric and carcass layers follows their real mean radius, i.e., the mean radius of the actual flexible pipe, but the equivalent approach implies different numerical and actual layers' thickness, causing the formation of "modeling" gaps, which can be observed in Figure 3-6.

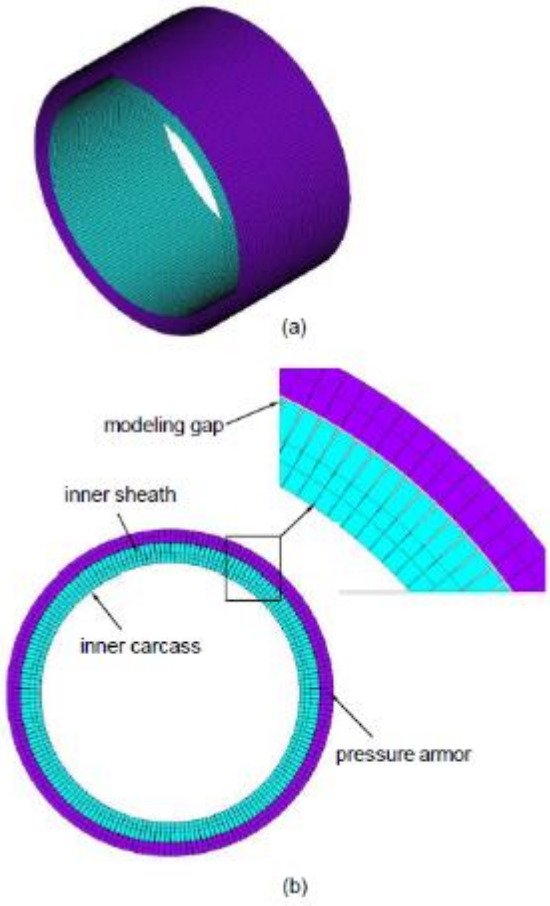

Figure 3-6: Finite Element Mesh (SOUSA *et al.* 2018)

This problem is circumvented by positioning the polymeric layer following its external diameter and increasing its equivalent thickness t_{e_s} to cover the existing gap. Moreover, the Young modulus has to be adjusted to maintain the equivalent layer stiffness, following Eq. (36).

$$t_{e_s} = t_s + \left(\frac{t_c - t_{e_c}}{2}\right) \tag{35}$$

$$E_{e_s} = \frac{t_s}{t_{e_s}} \cdot E \tag{36}$$

where t_s and t_c the thickness of the polymeric layer and the interlocked carcass in the actual pipe, respectively, t_{e_c} is the equivalent thickness of the interlocked carcass.

Additionally, the contact elements placed over the pressure armor must be moved to align with the elements positioned over the inner polymeric layer and preserve the real interaction location in the actual pipe.

Following what was discussed in Sections 3.1 to 3.5, the FE mesh is generated considering the nodal coordinates defined by Eqs. (37) to (40), which are then linked to form the layers' FE meshes. After that, the contact elements are placed, and the boundary conditions and pressure loading are imposed. The developed APDL macro controls all of these processes.

$$X_{i+(j-1)\cdot n_{cd\,k},k} = \frac{L_t}{n_{ld\,k}}(j-1) \tag{37}$$

$$Y_{i+(j-1)\cdot n_{cd\,k},k} = \{1 + o_k \cdot \cos\left[2\theta_{i+(j-1)\cdot n_{cd\,k},k}\right] \cdot r_{ml\,k} \cdot \cos\left[\theta_{i+(j-1)\cdot n_{cd\,k},k}\right] \tag{38}$$

$$Z_{i+(j-1)\cdot n_{cd\,k},k} = \{1 + o_k \cdot \cos\left[2\theta_{i+(j-1)\cdot n_{cd\,k},k}\right] \cdot r_{ml\,k} \cdot \sin\left[\theta_{i+(j-1)\cdot n_{cd\,k},k}\right] \tag{39}$$

$$\theta_{i+(j-1)\cdot n_{cd\,k},k} = \frac{\theta_{ml}}{n_{cd\,k}}(i-1) \tag{40}$$

where $i = 1 \ldots n_{cd\,k}$ e $k = 1 \ldots n_{ml}$, being n_{ml} the number of layers of the FE model, r_{ml} the layer's radius in the FE model and θ_{ml} is the angular length.

Finally, as this problem is related to structural instability, the arc-length method (or Ricks' method) was used in the problem solution. In addition, the initial applied load was equivalent to 2% of the external applied load, in this case the carcass' elastic collapse

pressure (Eq. (4)). In the same way that SOUSA et al. (2018) proposed, a stopping criterion was used to reduce the computational cost of the analysis. In the present work, the chosen criterion was 10% of the nodal displacement relative to the most internal layer mean radius. In some cases, the stopping criterion had to be modified to a maximum of 15%.

3.7 Case Study

This section compares the bisymmetric and symmetric collapses of a 2.5" flexible pipe whose main characteristics are presented in Table 3-2. Aiming at differentiating both collapse mechanisms, the ovalization values o used were 0.1%, 0.2%, 0.5%, 1%, 2%, 3%, and 4%, the effective stress values for the interlocked carcass σ_{ef}^{c} were 200 MPa, 300 MPa, 400 MPa, 500 MPa, 600 MPa, and 700 MPa. For the effective stress of the pressure armor σ_{ef}^{p}, the values were 200 MPa, 400 MPa, 600 MPa, 800 MPa, and 900 MPa. The effective stress was defined using the proposition presented in Section 2.1, and in the finite element model represents the material's yield stress.

These parameters were combined, creating a matrix of 210 finite element analyses. The results of this matrix of cases were compared to those obtained with the numerical model considering the wet bisymmetric collapse.

Table 3-2: Case of Study Structure Parameters

Parameter	Value
Internal diameter (in)/(mm)	2.5/63.5
Carcass thickness (mm)	4.00
Pressure sheath thickness(mm)	4.00
Pressure armor thickness (mm)	6.20
Carcass cross-section area (mm²)	25.60
Pressure armor cross-section area (mm²)	53.53
E pressure sheath (MPa)	3.50E+02
E carcass (MPa)	1.93E+05
E pressure armor (MPa)	2.05E+05
Carcass Poisson coefficient	0.30
Pressure sheath Poisson coefficient	0.45
Pressure armor Poisson coefficient	0.30

3.7.1 Bisymmetric Collapse

Taking as an example an analysis with an ovalization of 0.1%, effective stress of the carcass σ_{ef}^{c} and pressure armor σ_{ef}^{p} of 200 MPa, Figure 3-7 shows the calculated pressure vs. ovalization curve. This figure shows a nonlinear increase in load until it reaches its peak at 14.75 MPa. After this peak, the structure is in an unstable state, with an increase in ovalization even with a decrease in load. Thus, the maximum collapse pressure is considered the bisymmetric collapse pressure of this analysis, i.e, the load that destabilizes the structure.

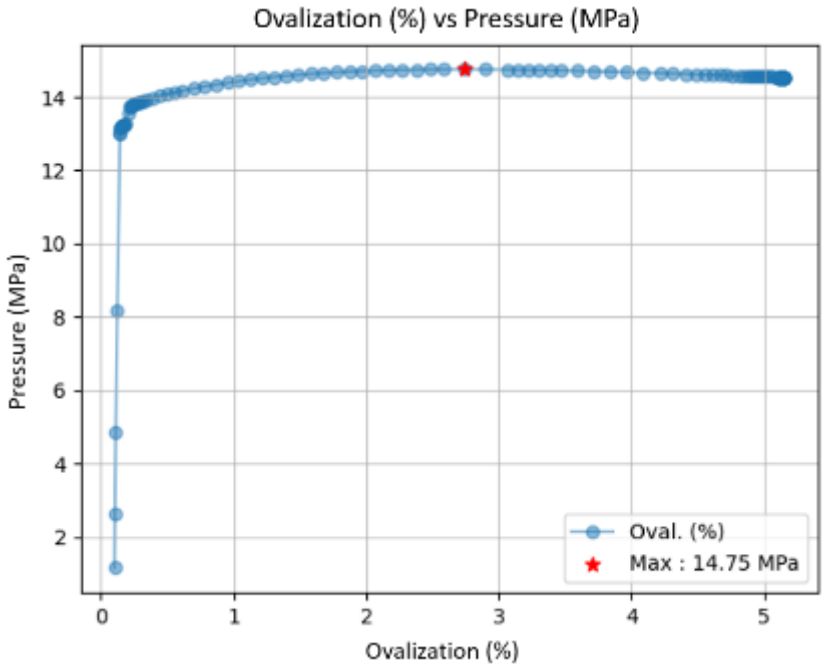

Figure 3-7: Pressure vs Ovalization Curve for $o = 0.1\%$, $\sigma_{ef}^{c} = \sigma_{ef}^{p} = 200\ MPa$ – Bisymmetric Collapse

Figure 3-8 shows the nodal displacements' distribution at the collapse load, while Figure 3-9 shows these nodal displacements at the end of the analysis. Both figures have their deformation scaled by 5 for better visualization. It is observed that this structure begins to collapse with an ovalization value of 2.74% (Eq. (5)), showing the "eight" shape of the bisymmetric collapse (Figure 3-9).

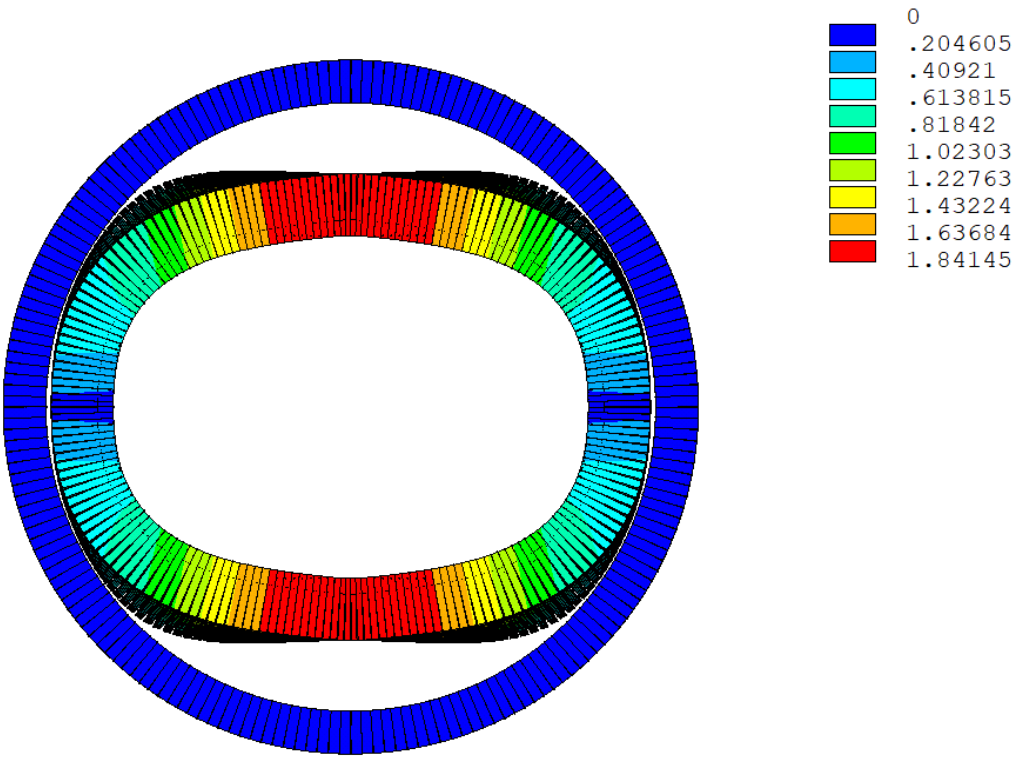

Figure 3-8: Nodal Displacements (mm) at Collapse Pressure – Bisymmetric Collapse

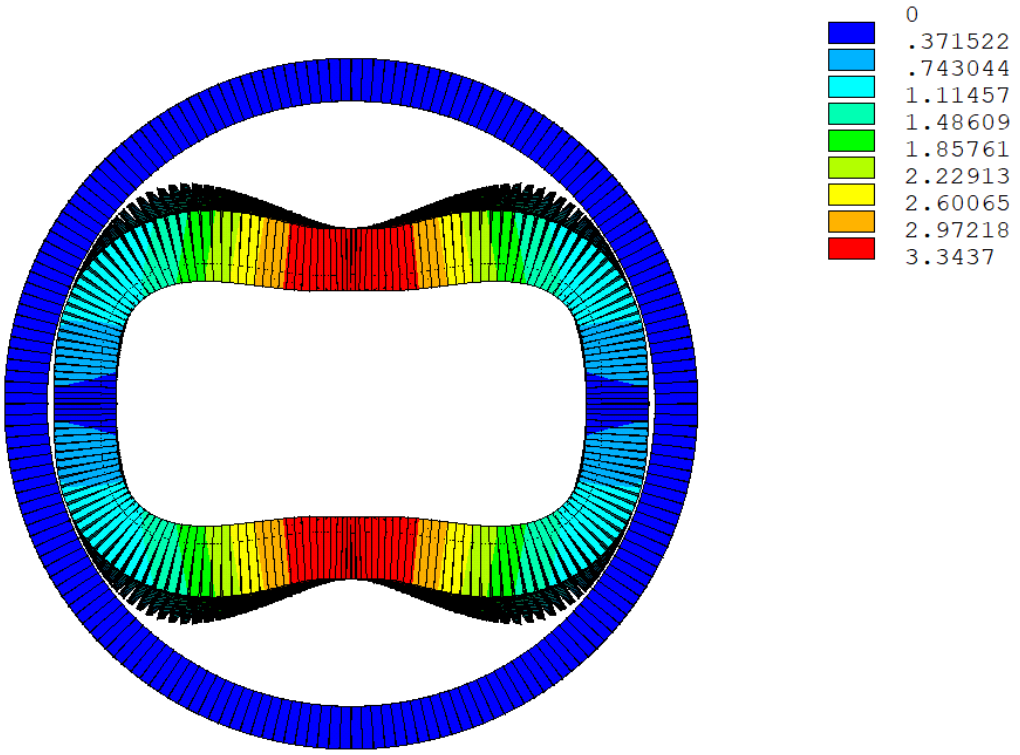

Figure 3-9: Nodal Displacements (mm) at Analysis End – Bisymmetric Collapse

Regarding the stresses, Figure 3-10 shows the von Mises stresses in the layers at the collapse pressure, and Figure 3-11 illustrates the stresses at the end of the analysis.

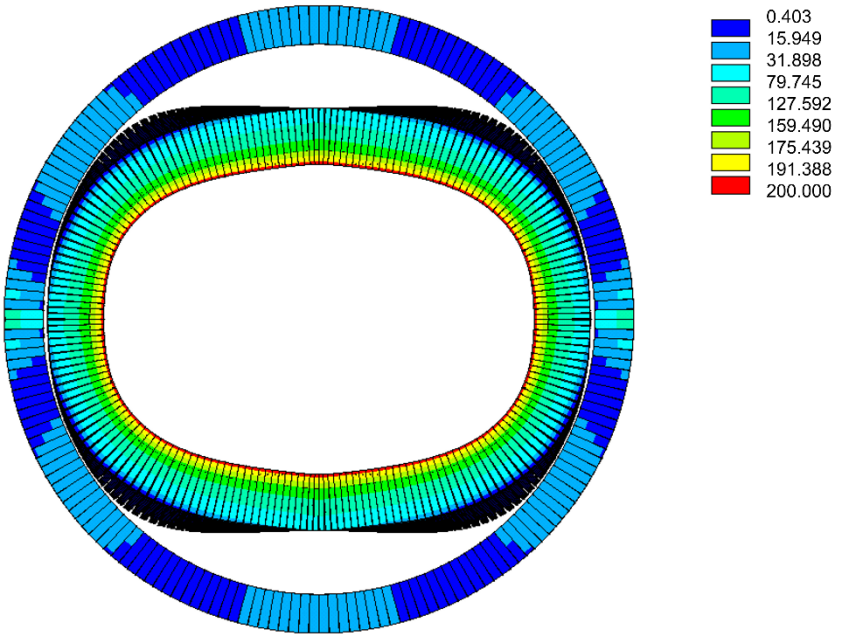

Figure 3-10: Stress Distribution (MPa) at Collapse Pressure – Bisymmetric Collapse

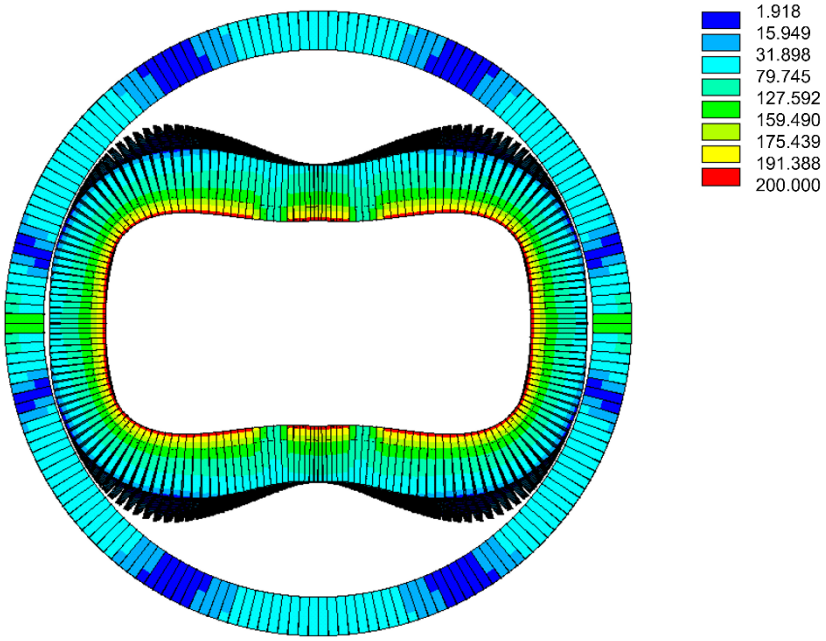

Figure 3-11: Stress Distribution at Analysis End – Bisymmetric Collapse

As shown in Figure 3-10 and Figure 3-11, the pressure armor stress state is elastic throughout the analysis. As the FE model proposed in this work uses layered shell elements (Section 3.6), the stress analysis in the carcass layer is detailed. Figure 3-12 shows the stress ratio for the carcass bottom, middle, and top fibers, where the stress ratio 1 means that the fiber reached the yield stress. This figure shows the load progression for 18.99% and 58.53% of the calculated collapse pressure.

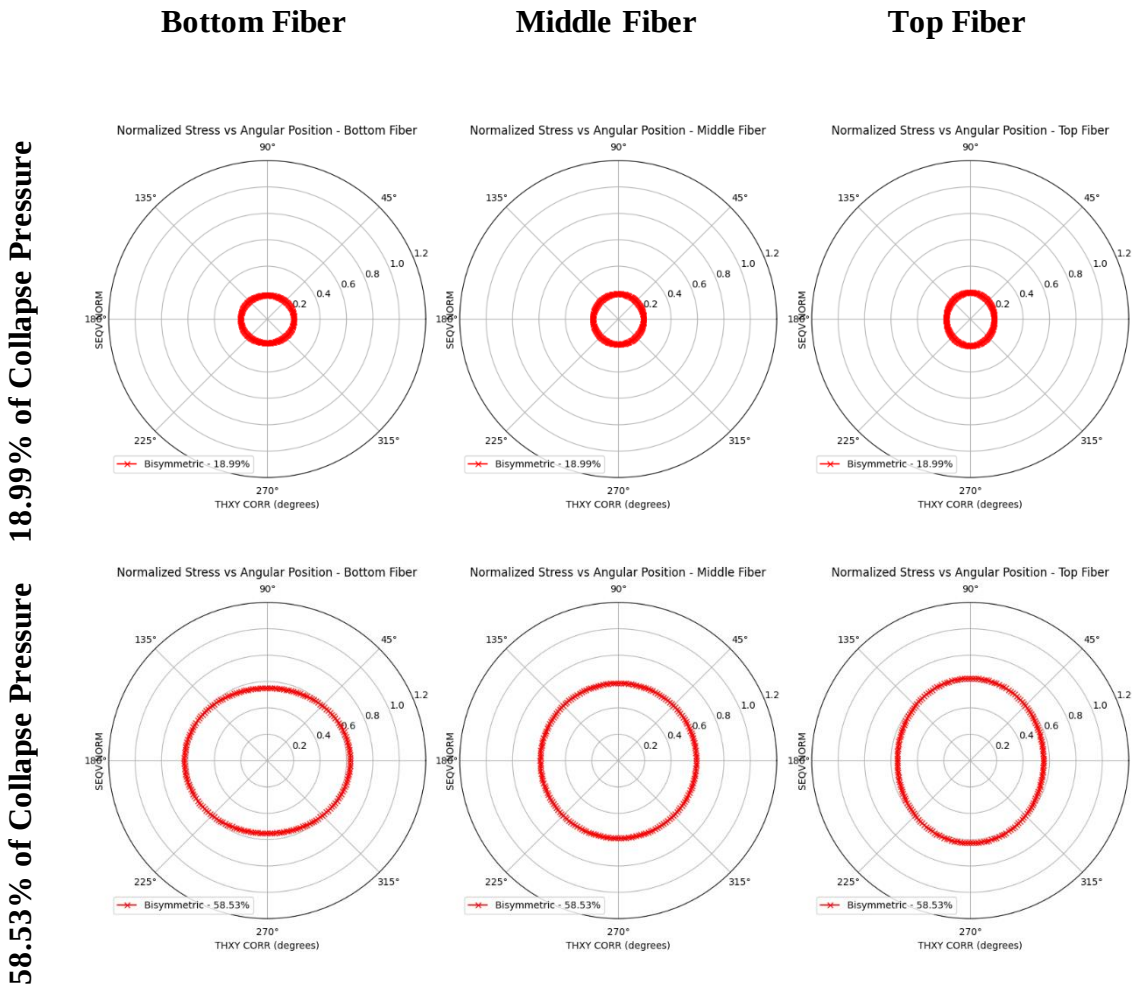

Figure 3-12: Stress Ratio – Load Progression

Figure 3-12 shows that the bottom fibers have slightly higher loads in $\theta_{ml} = 0°$ and $\theta_{ml} = 180°$ than for $\theta_{ml} = 90°$, $\theta_{ml} = 270°$.On the other hand, the top fibers show the complete opposite behavior. The middle fibers show a balanced loading throughout all angular positions. Hence, the bending effects in these figures are small.

To analyze the collapse occurrence, Figure 3-13 shows the stress ratio for a step right before the collapse occurrence, with 93.16% of the collapse pressure and at collapse.

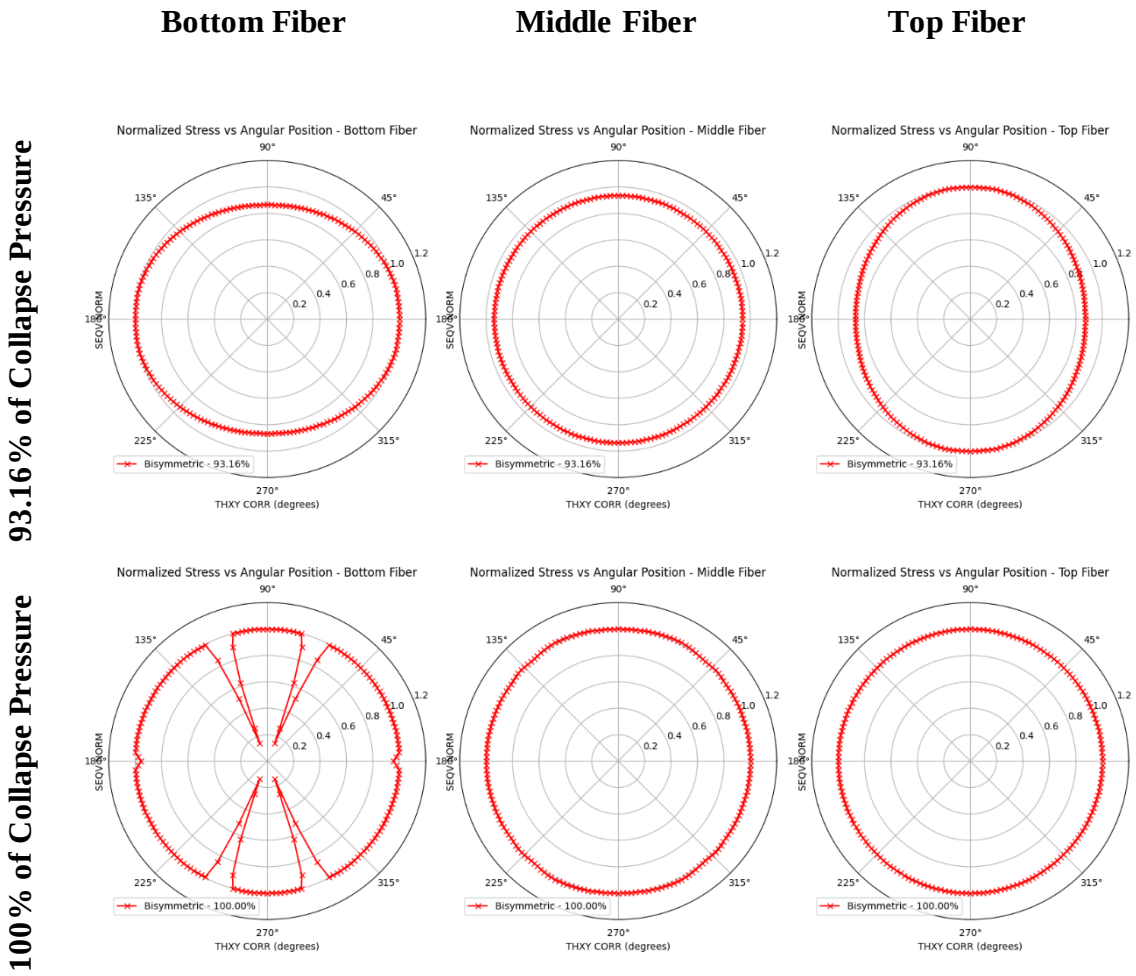

Figure 3-13: Stress Ratio – Collapse Pressure

The previously noticed behavior regarding the bottom, middle and top fiber loading are still present right before the structure collapse. The collapse occurs, in this case, when the carcass middle fiber reaches the yield stress, while the bottom fiber shows the forming of four plastic hinges as defined by the angular position intervals [-61.88º,61.88º], [76.88°,103.12º], [118.12º,241.88º] and [256.88º, 298.12º]. The top fiber also reaches the yield stress limit throughout the angular length.

3.7.2 Symmetric Collapse

Using the same flexible pipe of Section 3.7.1, Figure 3-14 shows the pressure vs. ovalization curve for the case of symmetric collapse. Compared to bisymmetric collapse, this failure mode reached its maximum collapse pressure at a lower ovalization value of 1.31% (Eq. (5)). The graph also shows a smoother load progression in this analysis. The collapse pressure for this failure mode was 13.95 MPa, slightly lower than the bisymmetric case.

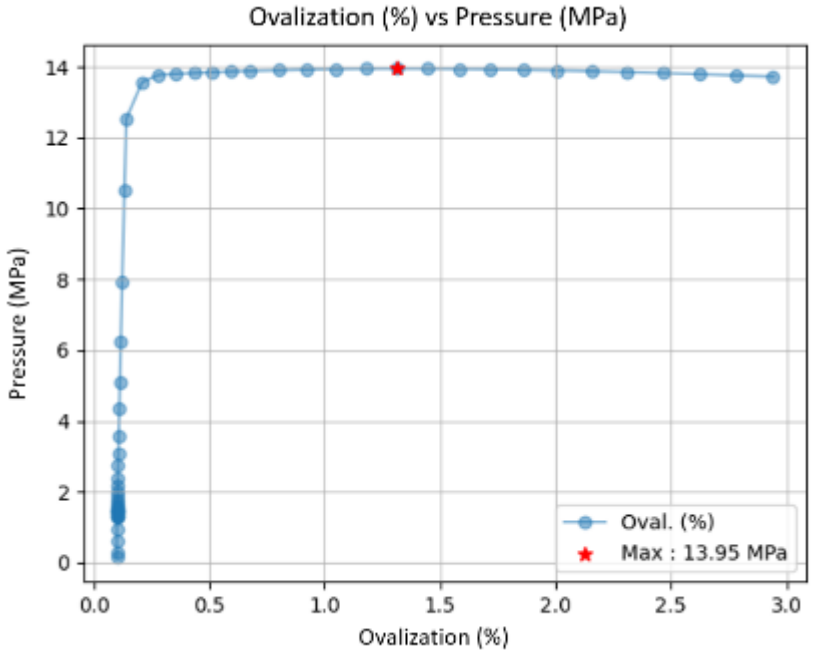

Figure 3-14: Pressure vs Ovalization Curve for $o = 0.1\%$, $\sigma_{ef}^{c} = \sigma_{ef}^{p} = 200\ MPa$ – Symmetric Collapse

When analyzing the displacement at the structure's collapse load, in Figure 3-15, the symmetric "heart" shape can be observed, reaching a lower ovalization (1.31%) compared to the bisymmetric collapse (2.74%), which can be explained by the restriction at the $\theta_{ml} = 270°$ nodes due to the contact with the pressure armor. This behavior is maintained when observing the post-failure mode of the structure in Figure 3-16.

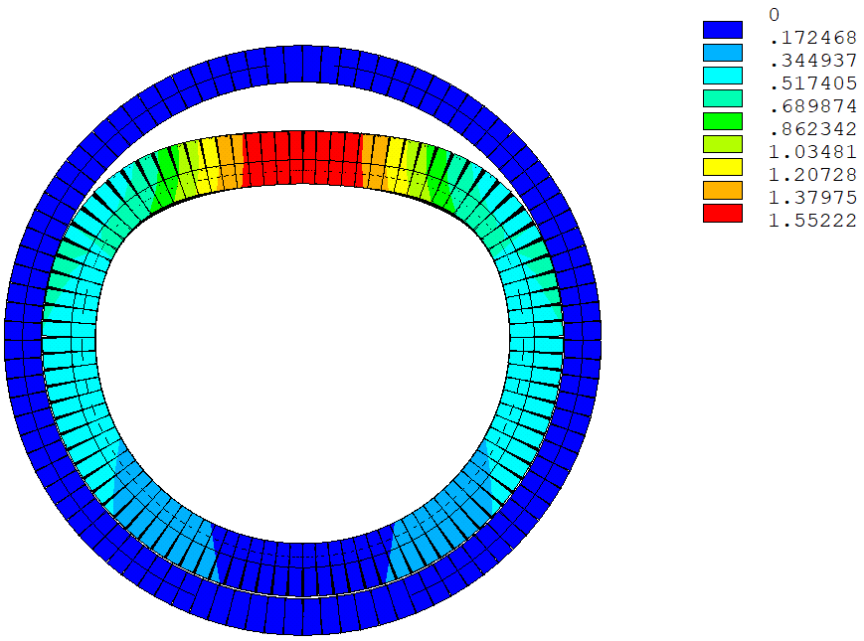

Figure 3-15: Nodal Displacements (mm) at Collapse Pressure – Symmetric Collapse

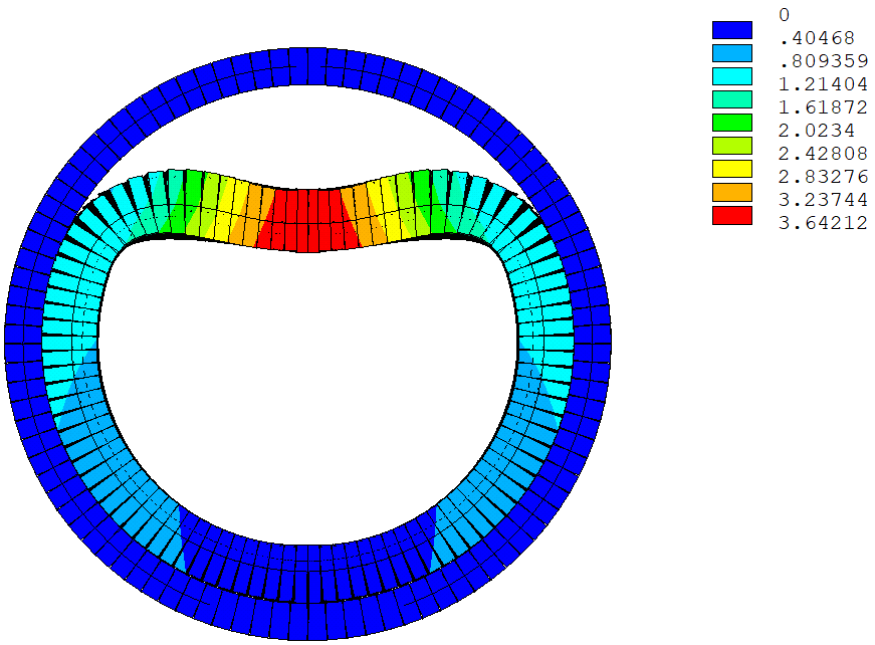

Figure 3-16: Nodal Displacements (mm) at Analysis End – Symmetric Collapse

Similarly to what is shown in Section 3.7.1, the stress analysis for the symmetric collapse pressure relies again on the stress ratio of the carcass. In Figure 3-17, the load progression between 19.78% and 55.15% of the collapse pressure shows similar behavior to the bisymmetric collapse results discussed in Section 3.7.1.

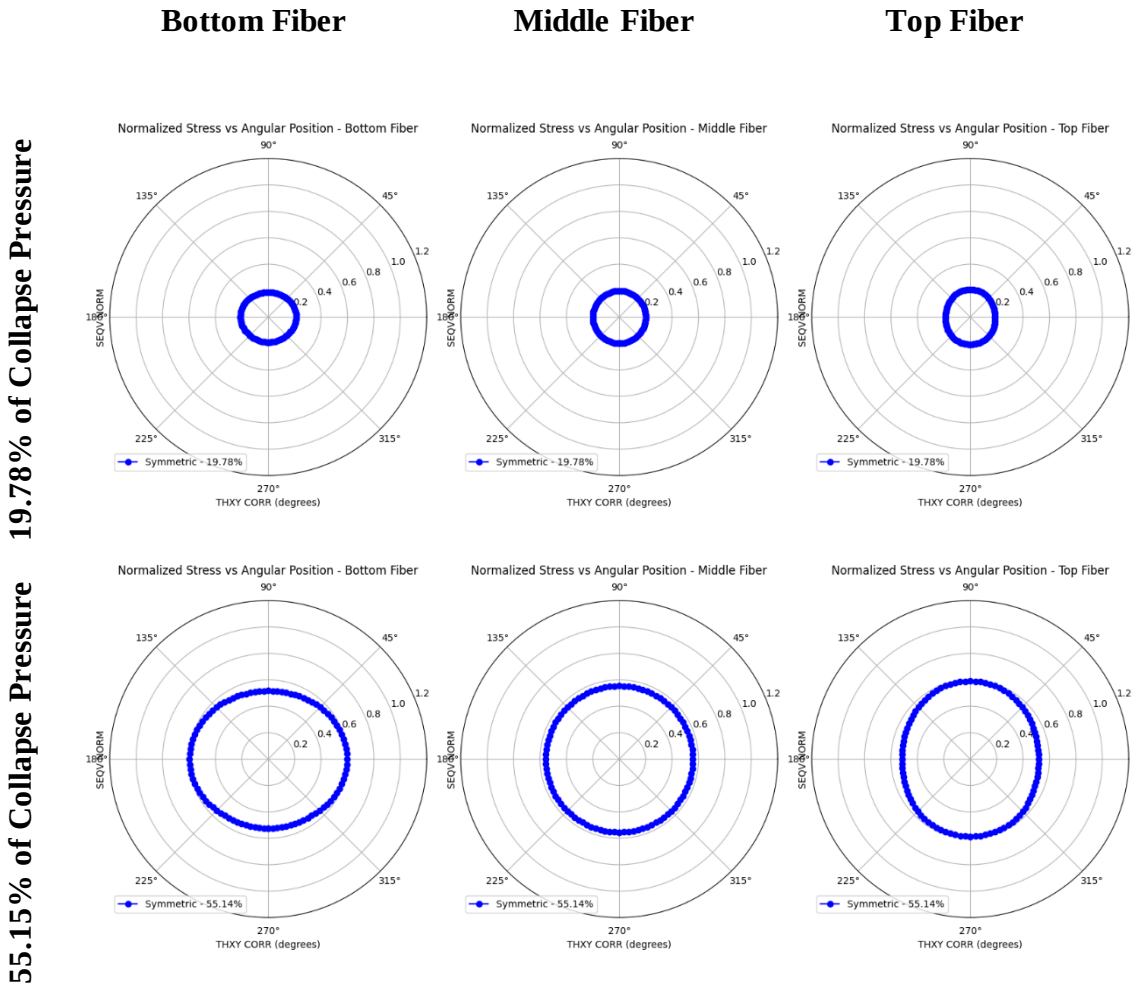

Figure 3-17: Stress Ratio – Symmetric Collapse

The main difference between bisymmetric and symmetric collapse modes arises when analyzing Figure 3-18, which compares a load of 96.50% of the collapse pressure with the load at which the collapse occurs. It is possible to notice an unloading of the bottom fibers between θ_{ml} =45º and θ_{ml} =135º, while the top fiber reaches the yield limit in this same angular position. Also, Figure 3-18 shows once again the collapse occurring when the middle fibers reaches the yield stress limit, but the bottom fiber plastic rings appear in the angular interval of [127.75º, 52.5º] and [78.75º, 101.25º]. Figure 3-19 shows the comparison between bisymmetric and collapse failure modes stress ratios.

Bottom Fiber **Middle Fiber** **Top Fiber**

96.50% of Collapse Pressure

100% of Collapse Pressure

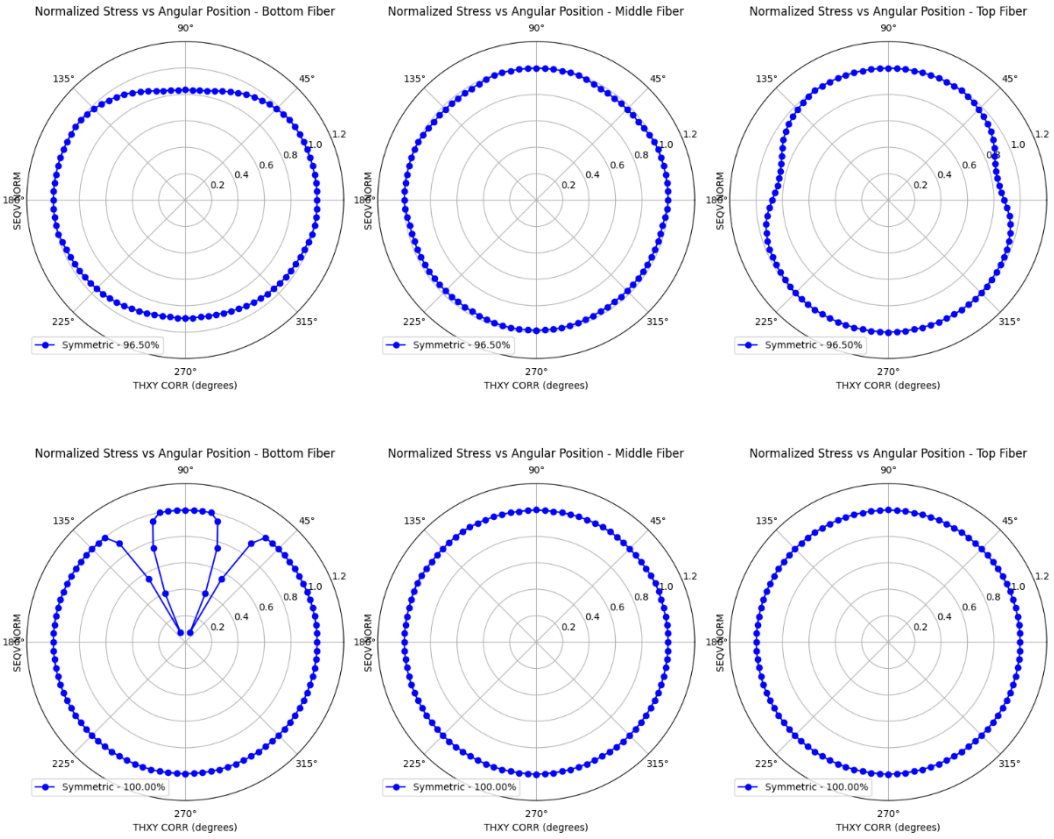

Figure 3-18: Stress Ratio – Symmetric Collapse

Bottom Fiber **Middle Fiber** **Top Fiber**

100% of Collapse Pressure

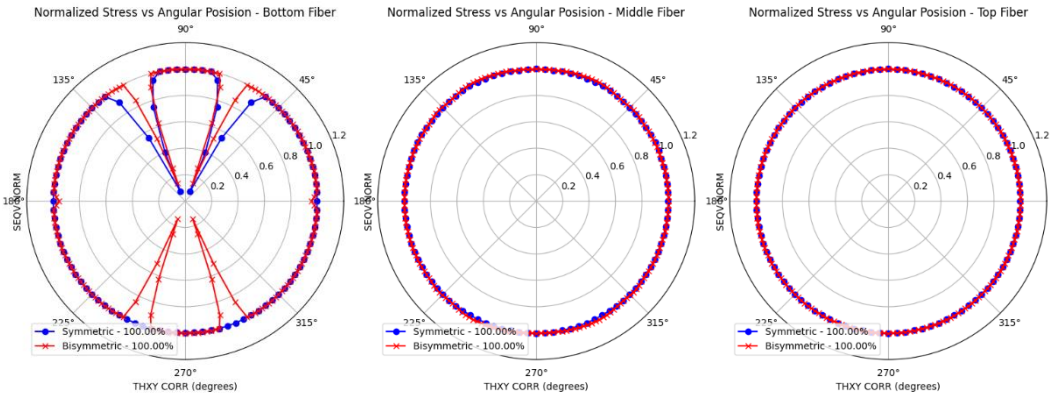

Figure 3-19: Bissymetric vs Symmetric Stress Ratio @ Collapse Pressure

Once again, Figure 3-19 highlights the differences between the bottom fibers' plastic hinges between symmetric and bisymmetric collapse modes but also shows similarities regarding the stress ratios for middle and top fibers. It is also noticed that the plastic hinge in the angular length [76.88°,103.12º] is quite similar between the two collapse modes.

For the symmetric collapse analysis, the complete analysis matrix results are shown in Figure 3-20 to Figure 3-24, showing the collapse pressure values vs. ovalization o (0.1%, 0.2%, 0.5%, 1.0%, 2.0%, 3.0% and 4%) for different values of effective stress of the carcass σ_{ef}^{c} (200 MPa, 300 MPa, 400 MPa, 500 MPa, 600 MPa and 700 MPa) and pressure armor σ_{ef}^{p} (200 MPa, 400 MPa, 600 MPa, 800 MPa and 900 MPa). Figure 3-20 to Figure 3-24 show the decrease of the collapse pressure with the increase of the ovalization values. This pattern is similar to the pressure armor effective stress (σ_{ef}^{p}) of 600 MPa, 800 MPa and 900 MPa. When observing Figure 3-20, it is noted a slightly increase of this decay for ovalizations equal to or greater than 2%, with a highlight for the curves of carcass effective stress (σ_{ef}^{c}) of 500 MPa, 600 MPa and 700 MPa. As expected, the ovalization plays an important part in the symmetric collapse evaluation: the higher the ovalization, the smaller the collapse resistance of the structure.

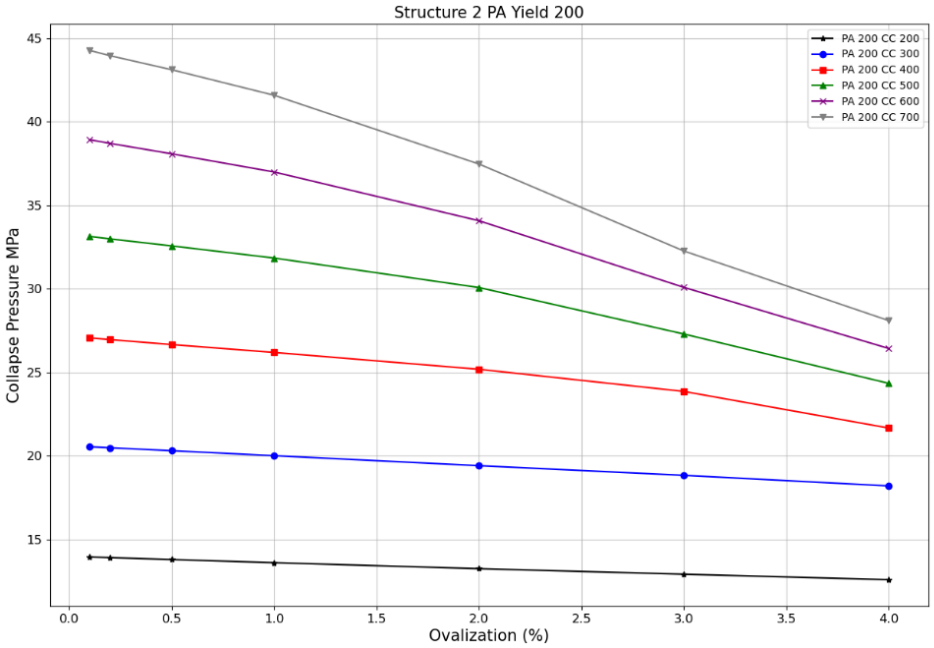

Figure 3-20: Symmetric Collapse Pressure vs Ovalization - $\sigma_{ef}^{p} = 200MPa$

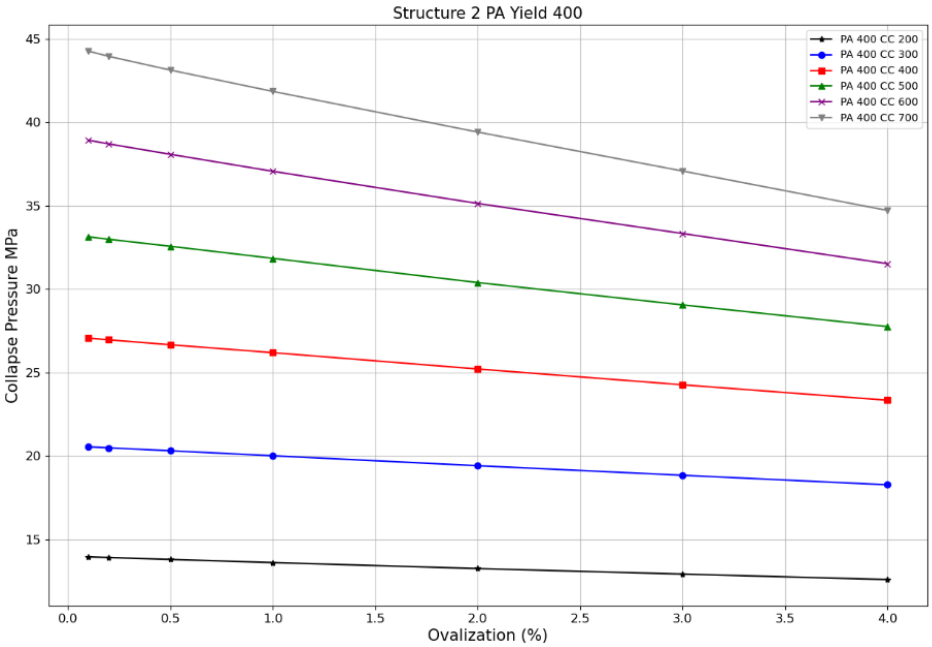

Figure 3-21: Symmetric Collapse Pressure vs Ovalization - $\sigma_{ef}^{p} = 400MPa$

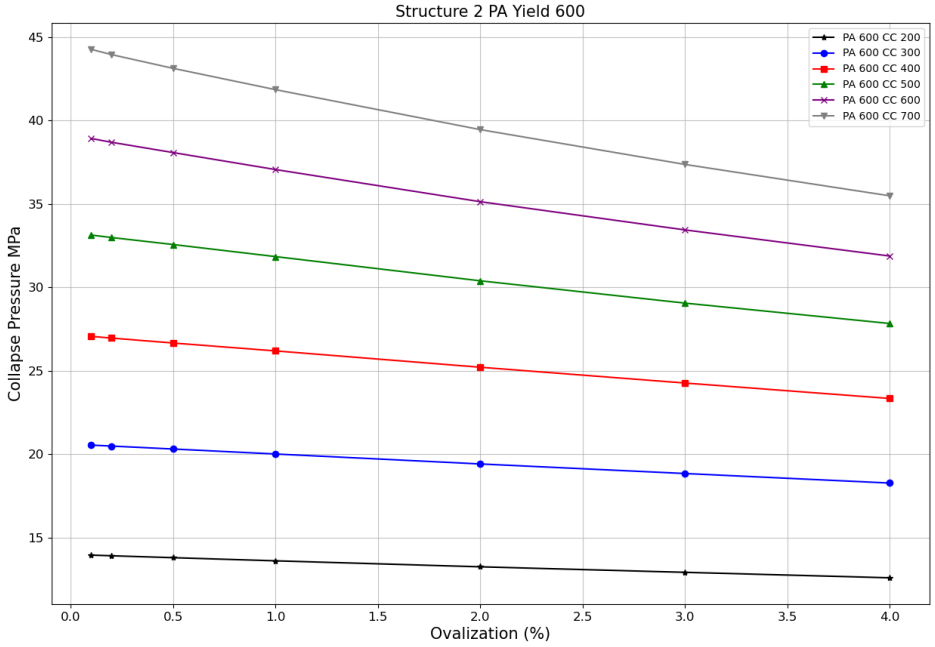

Figure 3-22: Symmetric Collapse Pressure vs Ovalization - $\sigma_{ef}^{p} = 600MPa$

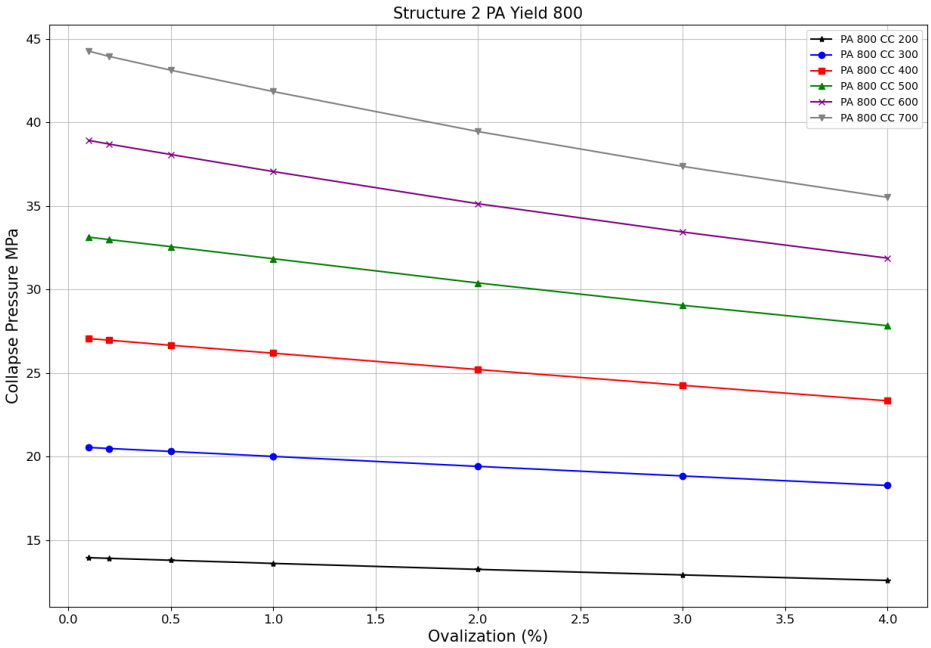

Figure 3-23: Symmetric Collapse Pressure vs Ovalization - $\sigma_{ef}^{p} = 800MPa$

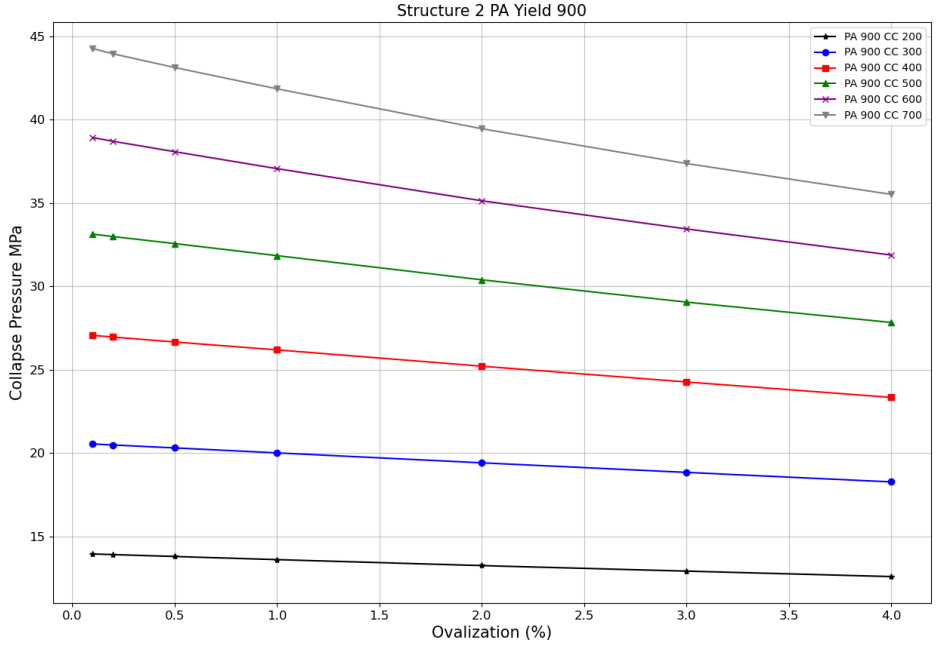

Figure 3-24: Symmetric Collapse Pressure vs Ovalization - $\sigma_{ef}^{p} = 900MPa$

The analyses of Figure 3-20 to Figure 3-24 indicates that for ovalization smaller than 1%, the collapse pressure behavior is identical for all pressure armor effective stress

(σ_{ef}^{p}) values. For ovalizations greater than 1%, the behavior of σ_{ef}^{p} of 200 MPa and 400 MPa are different from the others. This aspect reinforces the importance of ovalization in the symmetric collapse analysis, suggesting that the effect of the pressure armor's effective stress is more evident for higher ovalization values.

There are commonalities and differences when comparing the symmetric and bisymmetric hydrostatic collapse modes. The occurrence of the collapse when the middle fibers of the carcass reaches the stress limits is one point in common for both modes. On the other hand, the loading of the bottom and top fibers and the stress ratios differ between the two modes. Also, in this study, the symmetric collapse pressure is lower than the bisymmetric case, and the stress state of the pressure armor is elastic for both cases.

CHAPTER 4
SEMI-EMPIRICAL FORMULATION

This section briefly describes the symbolic regression technique and the methodology employed to derive an equation to predict the symmetric collapse pressure, relying on data from the previously presented FE model.

4.1 Symbolic Regression

Symbolic regression (SR) is a machine learning method that provides analytical equations from data, eliminating the need for prior knowledge about the investigated system (CHEN, LUO & JIANG, 2018). SR aims to generate mathematical expressions that describe relationships within data, bridging the gap between data, Machine Learning models, and scientific theories. This technique increases the explainability of the machine learning results once the analytical expressions can be evaluated and understood in detail. In most cases, SR employs genetic programming principles to evolve symbolic expressions (EIBEN & SMITH, 2015). Still, other approaches, such as simulated annealing (VAN LAARHOVEN & AARTS, 1987), are used, for example, in the TuringBot software (TURINGBOT, 2024) used in the present work.

TuringBot setup will be discussed further in Section 4.2, but its theory is briefly explained here. The core of SR is the combination of numerical operators, from the base forms (sum, subtraction, multiplication, division) to more complex ones, such as exponential, logarithmic, or logical functions. TuringBot (TURINGBOT, 2024) defines the following available operators:

- Arithmetic: addition, multiplication, division.
- Trigonometric: sin, cos, tan, asin, acos, atan.
- Exponential: exp, log, log2, sqrt, pow.
- Hyperbolic: sinh, cosh, tanh, asinh, acosh, atanh.
- Logical: smaller, greater, equal, different, logical_or, logical_and.
- History: delay, moving_average.
- Other: abs, floor, ceil, round, sign, mod, gamma, erf.

Simulated annealing is an optimization algorithm based on probabilities to approximate a global optimum of a given target. It is specially used when there is a possibility of multiple local optima (VAN LAARHOVEN & AARTS, 1987). This approach is used in SR to select the best probable analytical equation that explains the input-output relationship.

4.2 Dimensionless Parameters

As previously mentioned, TuringBot software is used in this work to generate the analytical equation. This section aims to detail the procedure used to acquire this equation.

The first step is to define the key parameters that govern the collapse mechanism. The proposition is to use dimensionless parameters as both input and output to TuringBot. This approach aids the parametric analysis of the equation while bringing clear domain definition to a problem with many variables involved. Furthermore, tests indicated that this strategy aids TuringBot in its search for the analytical equation.

As discussed in Section 3.7, ovalization is essential in this failure mode. Following what was proposed by SOUSA *et al.* (2022) for bisymmetric collapse analysis, the first parameter established is the dimensionless Π_o parameter, defined in Eq. (41).

$$\Pi_o = 1 + \frac{E \cdot t^2 \cdot r \cdot F_f}{2 \cdot EI_{eq}} \cdot o \tag{41}$$

where t is the layer thickness, r the mean radius, and F_f the fill factor (Eq. (2)); E is the layer material Young modulus and EI_{eq} is the equivalent bending stiffness (Eq. (3)) and o the ovalization (Eq. (5)).

Also, based on the preliminary conclusions discussed in Section 3.7, it is noted that the material effective stress σ_{ef} has an influence on the collapse strength of flexible pipes. With that in mind, the dimensionless Π_σ is defined in Eq. (42), based on the discussions of SOUSA *et al.* (2022).

$$\Pi_{\sigma} = \left(\frac{F_f \cdot t}{r}\right) \cdot \frac{\sigma_{ef}}{p_{el}} \quad \textbf{(42)}$$

where p_{el} is the elastic collapse pressure of an equivalent infinitely long orthotropic ring (Eq. (4)), F_f the fill factor (Eq. (2)), t is the layer thickness, r the mean radius and σ_{ef} the material effective stress.

The last dimensionless parameter defined is the Π_r, that correlates with the elastic collapse pressure (Eq. (4)) of the carcass (p_{el_C}) and the pressure armor (p_{el_P}). This proposal is inspired by previous studies discussed in Section 2.2, such SOUSA *et al.* (2022), where the stiffness ratio between carcass and pressure armor was identified as a critical parameter in determining the collapse mode of flexible structures. In this way, Π_r is defined by:

$$\Pi_{\mathrm{r}} = \frac{p_{el_C}}{p_{el_P}} \quad \textbf{(43)}$$

The analysis matrix chosen to feed the symbolic regression software comprises 14 structures, with its main characteristics shown in Table 4-1.

Table 4-1: Analysis Matrix Structures' Properties

Parameter	Carcass	Pressure Sheath	Pressure Armor
Internal diameter (mm)	63.5 to 304.8	63.5 to 304.8	63.5 to 304.8
Thickness (mm)	3.5 to 15.6	4 to 11.6	6.2 to 12
Cross-section area (mm²)	19.6 to 360	-	53.53 to 181.11
Young modulus (MPa)	1.93E+05	3.50E+02	2.05E+05
Poisson coefficient	0.30	0.45	0.30
Laying angle (deg)	86.87 to 88.38	-	85.67 to 88.44
Moment of inertia (mm⁴)	19.04 to 6421.57	-	114.29 to 1310.41

The final analysis matrix is defined by crossing the 14 structures with the ovalizations o of 0.1%, 0.2%, 0.5%, 1%, 2%, 3%, and 4%, effective stresses of the interlocked carcass σ_{ef}^{c} of 200 MPa, 300 MPa, 400 MPa, 500 MPa, 600 MPa, and 700 MPa, and effective stresses of the pressure armor σ_{ef}^{p} of 200 MPa, 400 MPa, 600 MPa, 800 MPa, and 900 MPa, yielding a total of 14 x 210 = 2940 FE analyses.

For each analysis of the cases matrix, the symmetric collapse pressure p_{sc} was evaluated with the FE model, and $\Pi_{p_{cr}}$ was calculated using Eq. (44)

$$\Pi_{\mathrm{p}_{cr}} = \frac{p_{sc}}{p_{el_C}} \tag{44}$$

Finally, for all 2940 cases, Π_{o} (Eq. (41)), Π_{σ} (Eq. (42)) and Π_{r} (Eq. (43)) were calculated for both the carcass and the pressure armor, and the TuringBot software was set to find the best symbolic regression equation that satisfies Eq. (45).

$$f^{*} = \arg \min_{f \in S_R} \sum_{i} \| f(\Pi_{\mathrm{o}}, \Pi_{\sigma}, \Pi_{r})_i - (\Pi_{\mathrm{p_{cr}}})_i \| \tag{45}$$

Table 4-2 shows the range of each dimensionless parameter of the analysis matrix.

Table 4-2: Dimensionless Parameters Ranges

Parameter	Mean	Std	Min	Max
$\boldsymbol{\Pi_{o_C}}$	2.1377E+00	1.0587E+00	1.0591E+00	4.8051E+00
$\boldsymbol{\Pi_{o_P}}$	2.4517E+00	1.4175E+00	1.0508E+00	6.4075E+00
$\boldsymbol{\Pi_{\sigma_C}}$	1.3013E+00	6.9678E-01	3.4427E-01	3.3651E+00
$\boldsymbol{\Pi_{\sigma_P}}$	2.4815E+00	1.7691E+00	2.2825E-01	7.6071E+00
$\boldsymbol{\Pi_{r}}$	1.5638E+00	1.3033E+00	2.7330E-01	4.3802E+00

From the operators detailed in Section 4.1, only the following were selected in the present work:

- Arithmetic: addition, multiplication, division
- Exponential: exp, sqrt

These choices were made to prevent overfitting the symbolic regression equation, a well-known problem in Machine Learning, where an over-complex model cannot generalize well to unseen data.

The search metric selected was the Root Mean-Squared Error (RMSE), with the train/test split set to 70% with random cross-validation. In this approach, 70% of the data was selected for training the symbolic regression equation and 30% for testing the equation for each model iteration. The cross-validation technique is especially recommended for small-data problems. Finally, the maximum formula complexity was set to 70, which means that maximum formula size in the search is set to 70 (TURINGBOT, 2024).

4.3 Analytical Equation

The resulting symbolic regression analytical equation that predicts the dimensionless collapse pressure $\Pi'_{\mathrm{p}_{cr}}$ is given by:

$$\Pi'_{\mathrm{p}_{cr}}(\overline{X}) = \frac{c_1 \times \left[\Pi_{\sigma_C} + \left(c_2 - \frac{c_3}{c_4 - \Pi_r}\right)\right]}{\sqrt{(c_5 + \Pi_r) \times f_2(\overline{X})) + c_{14}}} \quad \textbf{(46)}$$

$$f_2(\overline{X}) = \left(c_6 + \Pi_{\sigma_C}\right) \cdot \left\{c_7 + \left[c_8 \times \left(\Pi_{\sigma_C} - c_9 \cdot f_1(\overline{X})\right) + \Pi_{O_C}\right]\right\} + c_{13} \quad \textbf{(47)}$$

$$f_1(\overline{X}) = \left[\Pi_{O_C} + \left(\Pi_{\sigma_C} - c_{10}\right)\right] \cdot \left[\Pi_r - \Pi_{\sigma_C} \cdot \frac{\Pi_{O_P} - c_{11}}{\Pi_{\sigma_P}^2 + c_{12}}\right] \quad \textbf{(48)}$$

where the parameters $c_i, i = 1$ to 14 are presented in Table 4-3 and $\overline{X_i} = \langle \Pi_{O_P}, \Pi_{\sigma_P}, \Pi_{O_C}, \Pi_{\sigma_C}, \Pi_{\mathrm{r}} \rangle_i$.

Table 4-3: Parameters c_i, i=1 to 14

Parameter i	Constant	Parameter i	Constant
1	1.18663E+00	8	5.14148E-01
2	3.75486E-02	9	1.47810E-01
3	1.03849E-04	10	1.60170E+00
4	7.55795E-01	11	1.13832E+00
5	-1.48053E-01	12	2.52548E-02
6	6.98028E-02	13	1.44592E-01
7	-1.41354E+00	14	1.58692E+00

To evaluate the collapse pressure with its unit of measurement, Eq. (49) is used.

$$p'_{sc} = \Pi'_{p_{cr}} \cdot p_{el_C} \quad \textbf{(49)}$$

Based on the ranges shown in Table 4-2, SALib (IWANGA, USHER & HERMAN (2022)) was used to analyze the parameters' sensitivity presented in Table 4-4, where S1 and S2 are the first-order and second-order indices. S1 measures the contribution to the output variance using the single model parameter alone, and S2 measures the output variance contribution of the interaction between two model parameters. Finally, ST is the total indice that computes the contribution of S1 and higher other interactions (e.g., S2).

Table 4-4: Dimensionless Parameters Sensitivity

Parameter	ST	S1	S2 Π_{o_C}	S2 Π_{o_P}	S2 Π_{σ_C}	S2 Π_{σ_P}	S2 Π_r
Π_{o_C}	1.887E-01	1.688E-01	-	9.590E-04	1.392E-02	2.966E-03	9.360E-04
Π_{o_P}	1.751E-02	4.274E-03		-	-2.510E-04	8.019E-03	2.190E-04
Π_{σ_C}	4.414E-01	3.416E-01		-2.510E-04	-	1.724E-02	5.979E-02
Π_{σ_P}	8.909E-02	5.435E-02		8.019E-03	1.724E-02	-	6.250E-04
Π_r	3.829E-01	3.166E-01		2.190E-04	5.979E-02	6.250E-04	-

Figure 4-1 shows the graphic representation of S1 and ST sensitivity values for each dimensionless parameter. It is noticed that Π_{σ_C}, related to the carcass effective tension σ_{ef}, and Π_r, which correlates the elastic collapse pressures of the carcass and pressure armor, are the most important parameters regarding the Eq. (46) evaluation, having, respectively, S1 equals to 3.416E-01 and 3.166E-01, and ST equals to 4.414E-01

and 3.829E-01. These results indicate that these two parameters are vital to studying the symmetric collapse mode.

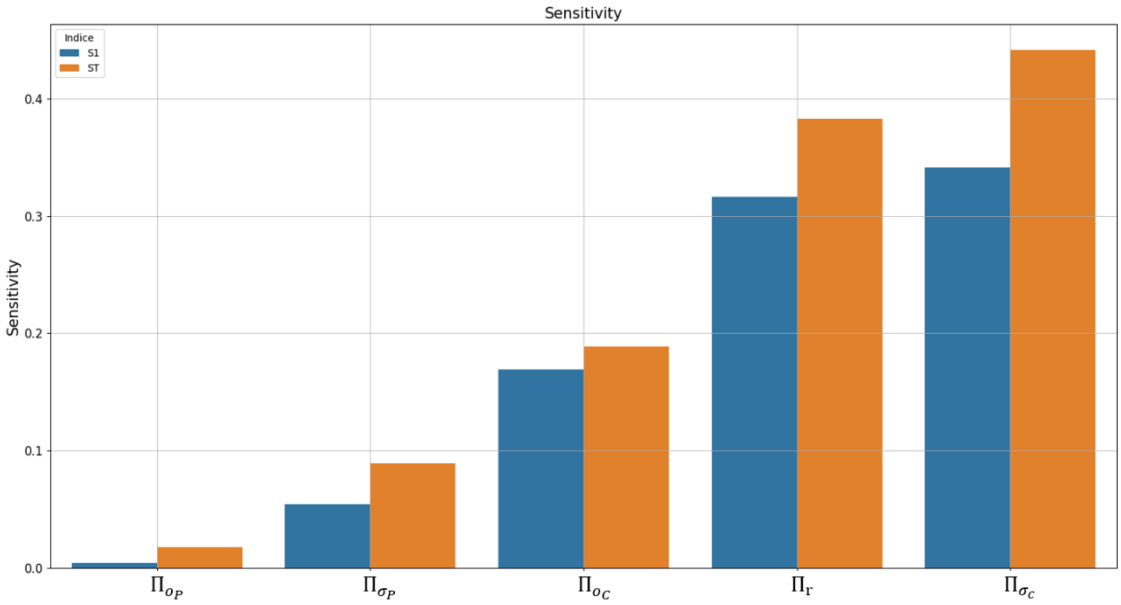

Figure 4-1: Dimensionless Parameters S1 and ST Analysis

Regarding S2 analysis, Figure 4-2 shows the values for each combined parameter. Even though the sensitivity values are in the order of E-02, again, the couple Π_{σ_C}, Π_r show its importance, with by far the most considerable S2 value of all, corroborating with the previous hypothesis of these two values being the most important for Eq. (46) and thus to symmetric hydrostatic collapse analysis.

The results obtained using the analytical equation are compared against the FE results. Gathering the results of the 2940 analysis matrix, the predicted dimensionless symmetric collapse pressure ($\Pi'_{p_{cr}}$) is compared with the collapse pressure acquired with the FEM, herein considered as the "true" values in Figure 4-3.

From Figure 4-3, it is possible to have a qualitative evaluation of the analytical equation that shows a good fit with the true values. In quantitative terms, the overall Mean Squared Error (MSE), Mean Absolute Error (MAE), R^2, and Pearson's correlation values are presented in Table 4-5.

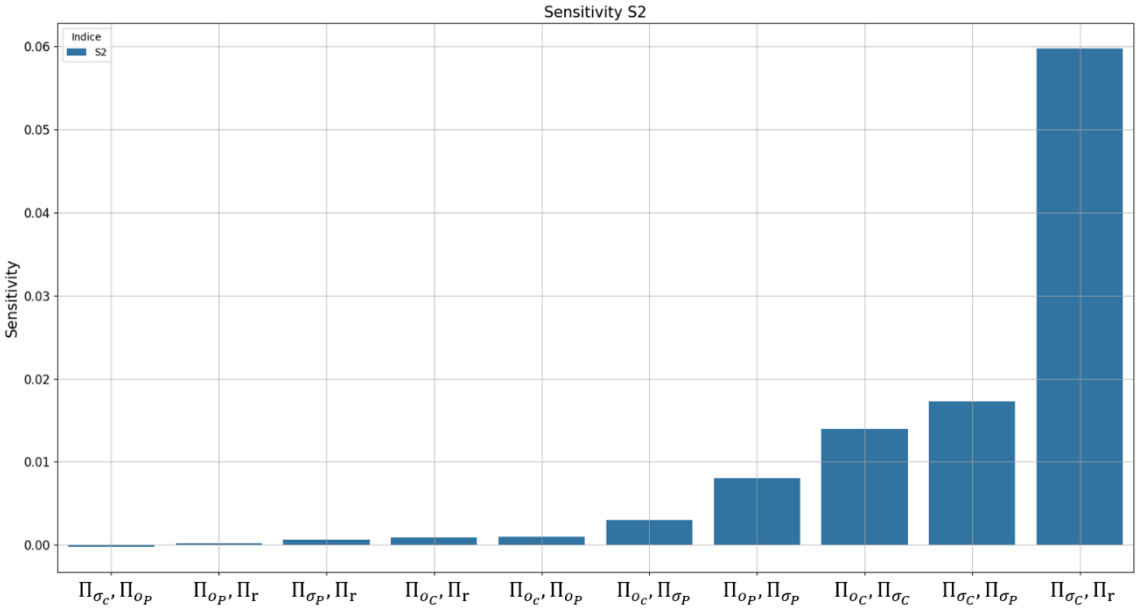

Figure 4-2: Dimensionless Parameters S2 Analysis

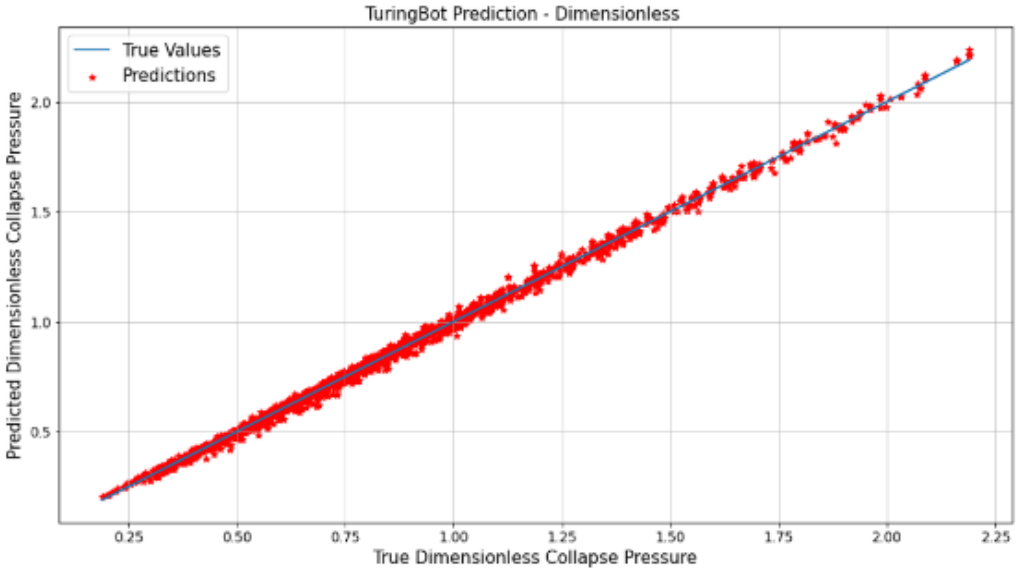

Figure 4-3: Predicted Dimensionless Symmetric Collapse Pressure

Table 4-5: Prediction Metrics

Parameter	Value
MSE	3.35E-04
MAE	1.40E-02
R^2	9.97E-01
Pearson's correlation	9.98E-01

Table 4-5 corroborates with the qualitative analysis, confirming that the analytical equation can predict the symmetric collapse pressure of flexible pipes with high reasonable agreement with high R^2 and correlation values (above 0.95) and very low MSE and MAE.

Generally, the residue analysis also indicates the quality of the model when evaluating surrogate models. Here, Eqs. (50) and (51) represent the residue and the percentual residue, respectively.

$$r_p = y_{pred} - y_{true} \tag{50}$$

$$p_{rp} = \frac{r_p}{y_{true}} \tag{51}$$

where y_{pred} is the predicted value, herein the symmetric collapse pressure calculated using the analytical equation, and y_{true} is herein the true value, i.e., the symmetric collapse pressure acquired from the FE analyses.

Figure 4-4 and Figure 4-5 show that the residue and percentual residue histogram, respectively, are centered around 0 in both cases, indicating that the prediction model performed well. In percentual terms, the smallest residue encountered is -13.83%, and the largest is $+9.11\%$, with Figure 4-5 showing lower occurrences of residue values near -10% and 10%.

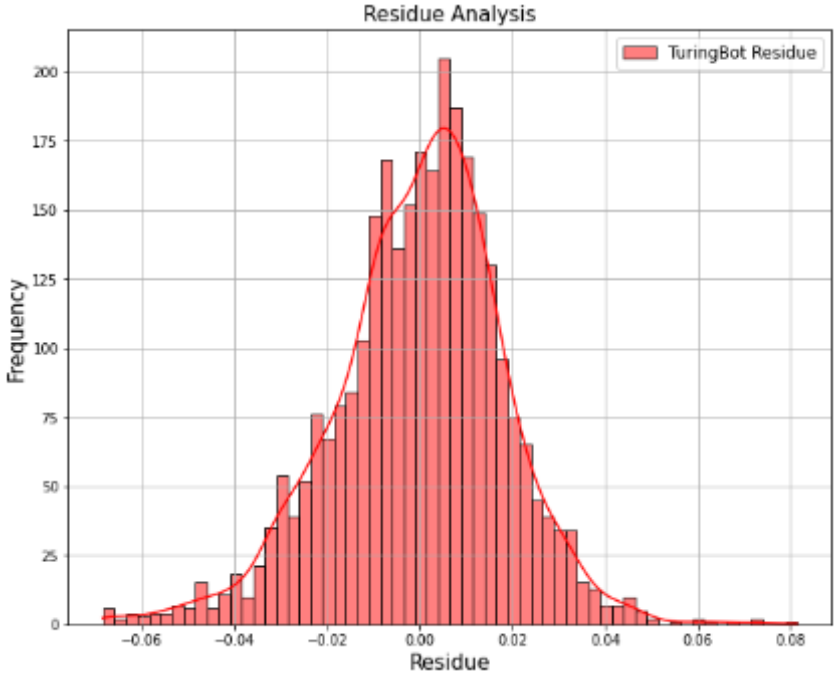

Figure 4-4: Prediction Residue Histogram

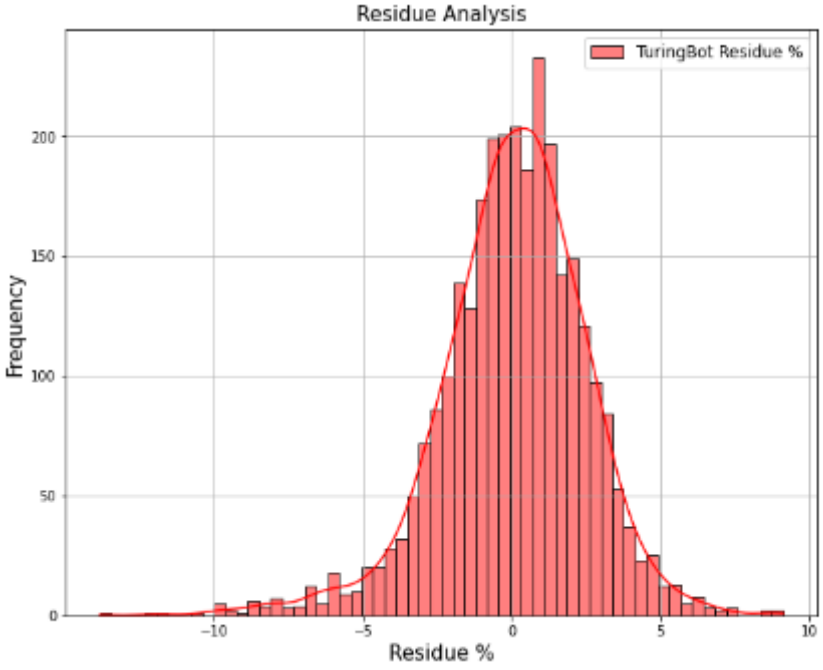

Figure 4-5: Prediction Percentual Residue Histogram

When analyzing the dimensional value of the collapse pressure, i.e., applying Eq. (49) to calculate the symmetric collapse pressure in MPa, it is clear that the high residue relies on smaller collapse pressure values within the 5-10 MPa range. Figure 4-6

shows that the higher the collapse pressure, the smaller the percentual residue, contributing to this prediction model's good fit.

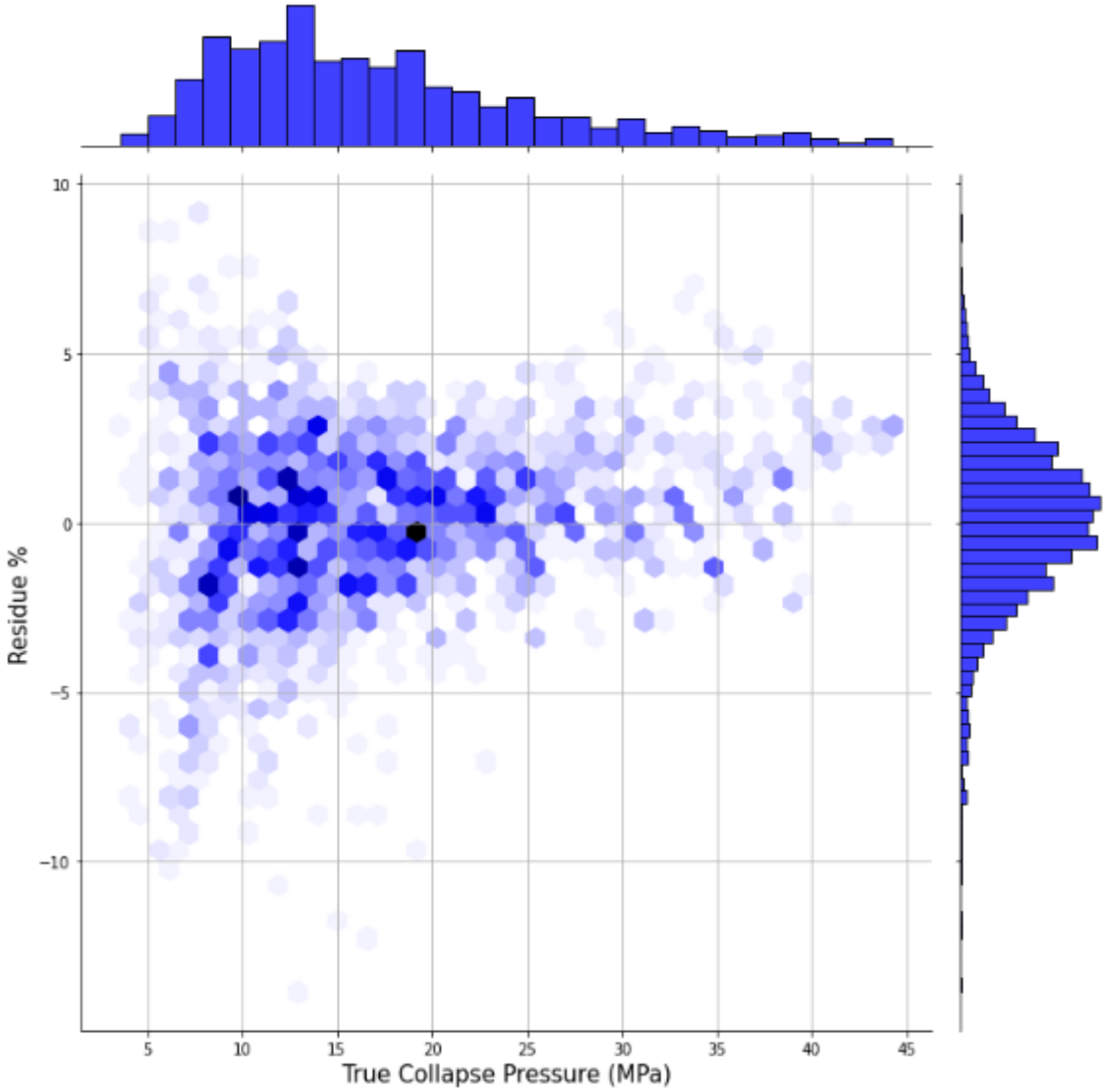

Figure 4-6: Percentual Residue Distribution vs Symmetric Collapse Pressure

CHAPTER 5
DISCUSSION

5.1 Analytical Equation Evaluation

This section evaluates the analytical equation against unseen data, i.e., data not used for the approximation model acquirement. The analysis matrix combined with a cross-validation methodology was employed to generate the symbolic regression equation. Hence, two other structures (herein structures 1 and 2), not used in the training procedure, were studied via the FE model and Eq. (46). The structures' characteristics are presented in Table 5-1.

Table 5-1: Structure 1 and 2 Characteristics

Parameter	Structure 1			Structure 2		
	Carcass	Pressure Sheath	Pressure Armor	Carcass	Pressure Sheath	Pressure Armor
Internal diameter (mm)	153.44	159.94	164.94	101.6	105.6	110.6
Thickness (mm)	6.5	5.0	8.4	4.0	5.0	6.2
Cross-section area (mm²)	90	-	91.68	32	-	50
Young modulus (MPa)	1.93E+05	3.50E+02	2.05E+05	1.93E+05	3.50E+02	2.05E+05
Poisson coefficient	0.30	0.45	0.3	0.30	0.45	0.3
Laying angle (deg)	87.80	-	87.90	87.58	-	87.20
Moment of inertia (mm⁴)	366.7	-	314.63	43.28	-	93.38

For both structures, the dimensionless parameters' ranges are presented in Table 5-2. It is essential to highlight that the validity of Eq. (46) relies on the dimensionless parameters selected to be within the range shown in Table 4-2, which is the case for structures 1 and 2.

Table 5-2: Dimensionless Parameter Ranges for Structure 1 and 2

Parameter	Min	Max
Π_{o_C}	1.0686E+00	4.3297E+00
Π_{o_P}	1.0729E+00	4.1768E+00
Π_{σ_C}	5.8286E-01	2.6569E+00
Π_{σ_P}	4.8076E-01	2.5575E+00
Π_r	3.3339E-01	6.1012E-01

Figure 5-1 compares the predicted symmetric collapse pressure against the FE values for structures 1 and 2. Again, this type of comparison is only qualitative, so the quantitative results are summarized in Table 5-3.

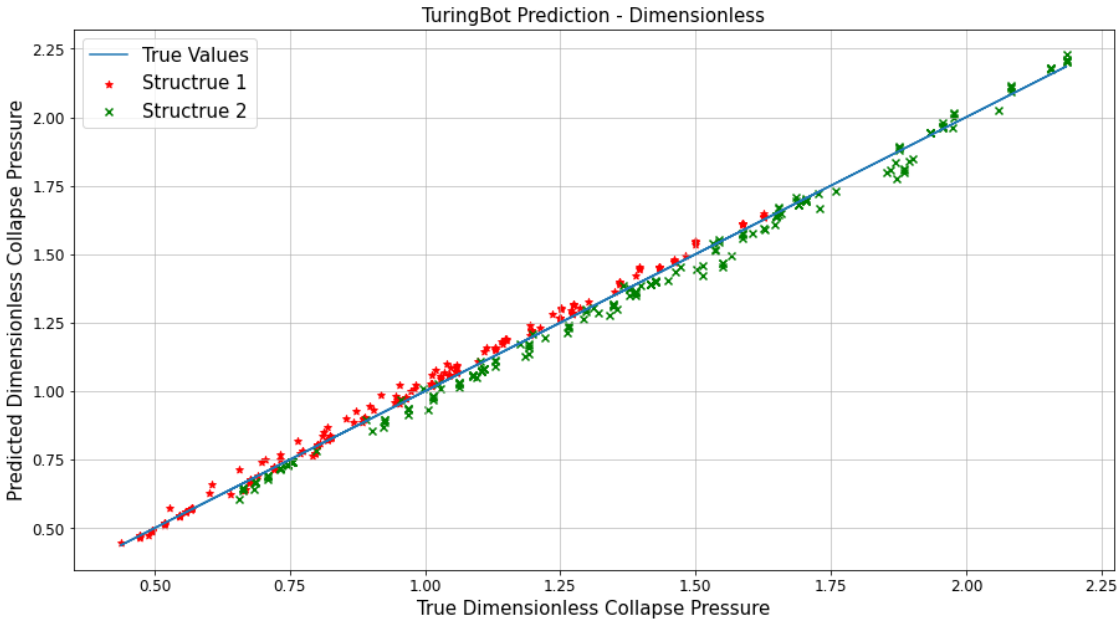

Figure 5-1: Predicted Dimensionless Symmetric Collapse Pressure – Structure 1 and 2

Table 5-3: Prediction Metrics for Structure 1 and 2

Parameter	Value
MSE	8.55E-04
MAE	2.32E-02
R^2	9.95E-01
Pearson's correlation	9.98E-01
Residue (Eq. (50))	Min: -9.6593E-02 Max: +7.0169E-02
Percentual Residue (Eq. (51))	Min: -7.94% Max: +8.79%

Both the qualitative comparison, shown in Figure 5-1, and the quantitative results, displayed in Table 5-3, show the quality of the symbolic regression model and its capability of generalizing to new data. Once compared to the training data results, the residue values are within the expected ranges.

5.2 Analytical Comparison

Using the equations proposed by SOUSA *et al.* (2022) (see APPENDIX A) to predict the bisymmetric wet hydrostatic collapse pressure for flexible pipes, this section compares these analytical results with the ones obtained with Eq. (46), the symmetric collapse analytical equation. Figure 5-2 shows the visual comparison between these results, where the 45° blue line represents the identity line where the symmetric collapse results are equal to the bisymmetric results.The green dots represent the bisymmetric values vs the symmetric ones.

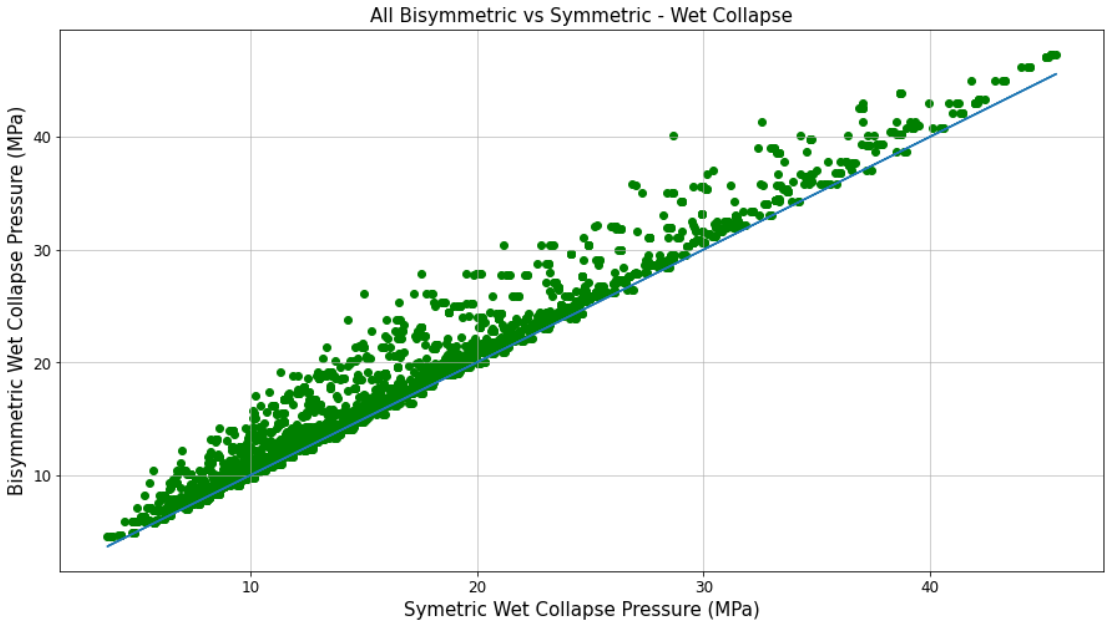

Figure 5-2: Bisymmetric vs Symmetric Wet Collapse Pressure

The analysis of Figure 5-2 corroborates with conclusions drawn in Section 3.7, as most cases yield a bisymmetric collapse pressure higher than the symmetric collapse pressure, represented by the green dots above the 45° blue line. In percentual terms, the cases where the bisymmetric collapse pressure is higher than the symmetric collapse pressure is 93.3%, leaving only 6.7% of the analysis where the bisymmetric collapse mode would require less energy than the symmetric mode. The latter is shown in Figure 5-3.

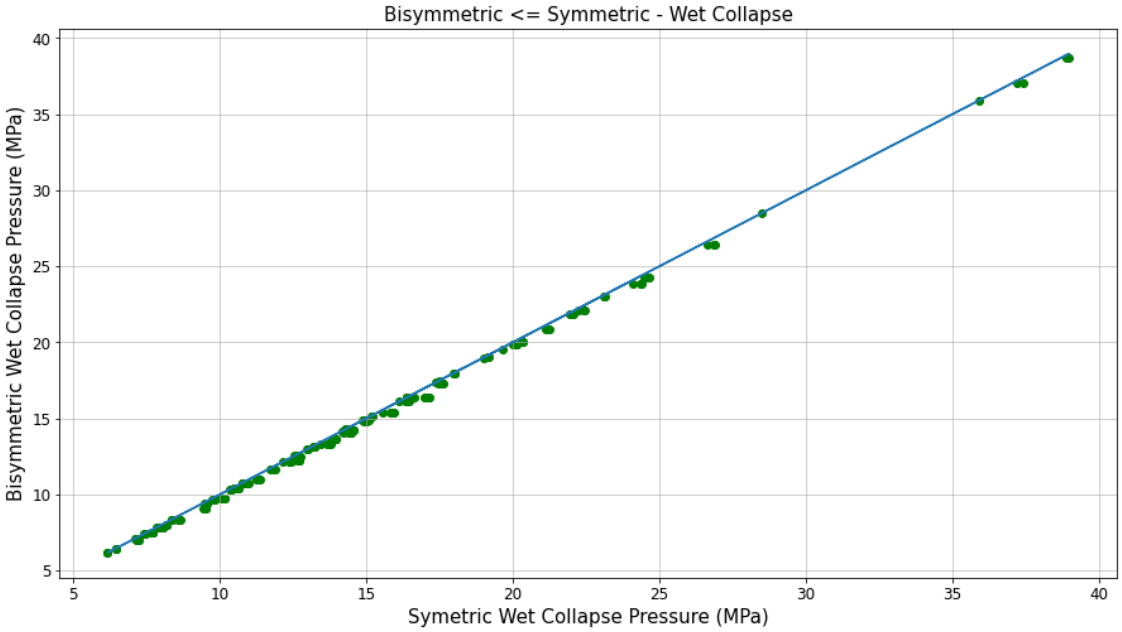

Figure 5-3: Bisymmetric ≤ Symmetric Wet Collapse Pressure

By analyzing Figure 5-3, it is possible to notice that even though the bisymmetric collapse pressure is lower than the symmetric collapse pressure, the values are close to each other, with a maximum difference of $0.79MPa$. Tha data presented in Figure 5-2 yields a R^2 value of 0.926 and a Pearson's correlation factor of 0.981, showing the strong relationship between bisymmetric and symmetric collapse results.

Figure 5-4 and Figure 5-5 corroborate that no clear distinction between the two failure modes can be made when crossing bisymmetric and symmetric collapse analytical results with the key parameters identified in Section 4.3 (Π_{O_C}, Π_{σ_C} and Π_r). This isolated analysis indicate that no parameter, alone, is capable of differentiate one collapse mode from the other.

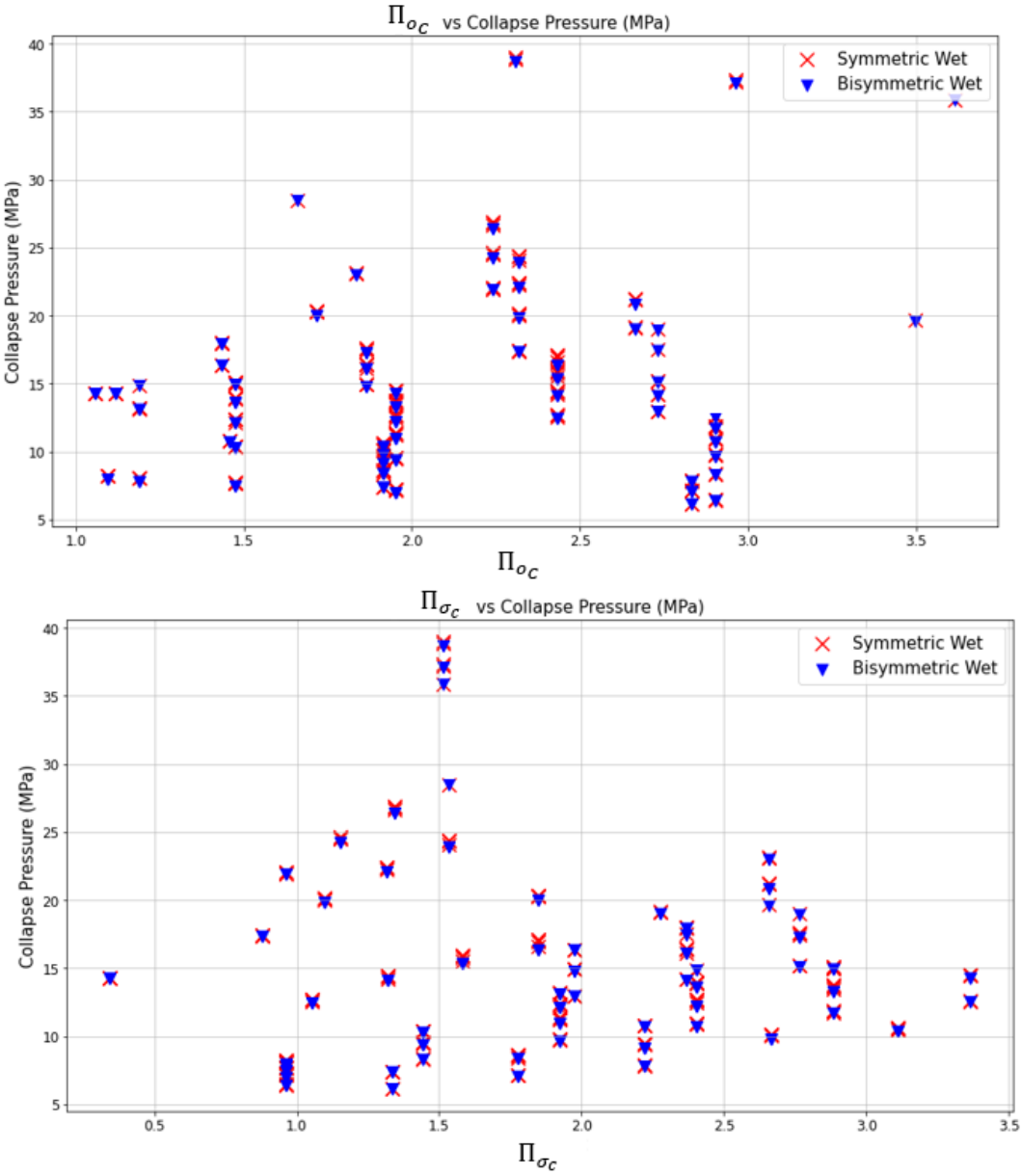

Figure 5-4: Collapse Pressure vs Dimensionless Parameters

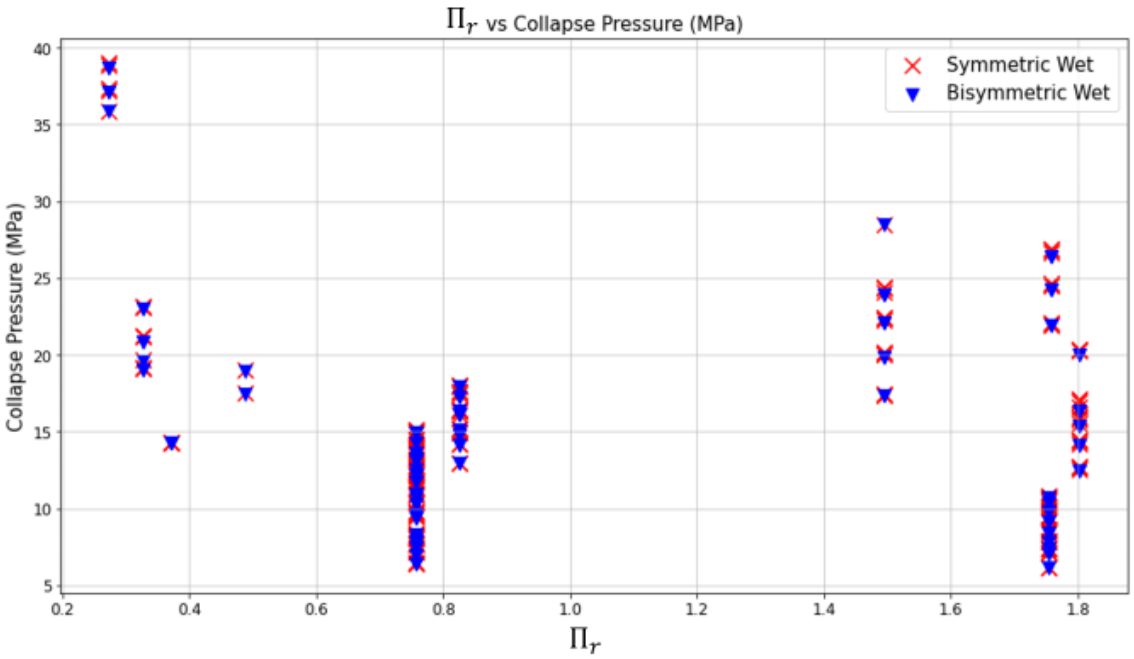

Figure 5-5: Collapse Pressure vs Π_r

To analyze the overall behavior, Figure 5-6 shows the comparison of the distributions of the Π_{oc}, $\Pi_{\sigma c}$ and Π_r parameters for the cases of bissymetric collapse pressure smaller than the symmetric (Figure 5-3) and the rest of the analyses. It is possible to see that for $\Pi_{\sigma c}$ no distinction is made between the two situations. Interesting observations can be inferred when checking the Π_{oc} and Π_r distributions. For these two parameters, Figure 5-6 indicates a limit for the cases where the symmetric collapse pressure is greater than the bisymmetric one, being $\Pi_{oc} < 3$ and $\Pi_r < 2$, suggesting that this could be a threshold when comparing bisymmetric and symmetric collapse results. For instance, the green point more distant from the 45° blue line in Figure 5-2 has $\Pi_r = 0.371$ and $\Pi_{oc} = 3.362$, indicating as $\Pi_{oc} > 3$ that the bissymetric collapse pressure is greater than the symmetric one, and in this case the structure would prefer to fail under a symmetric mode.

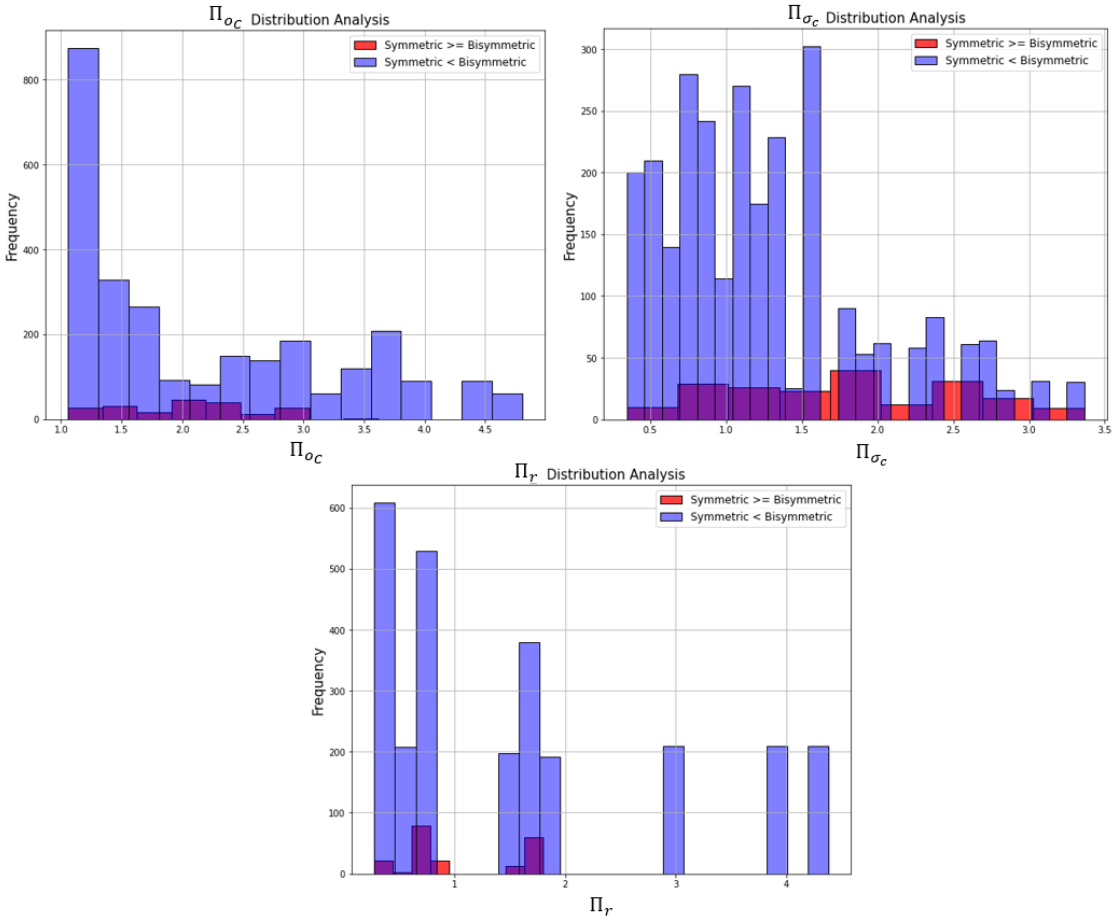

Figure 5-6: Dimensionless Parameters Histogram

CHAPTER 6
CONCLUSIONS

The first goal of this study was to conceive an FE model to evaluate flexible pipes' symmetric hydrostatic collapse. The proposal to introduce the symmetric imperfection via load unbalance was satisfactory in finding a methodology that would facilitate the parametric analysis and not be too heavily computationally costly. The symmetric collapse, as demonstrated in Section 3.7.2, occurs when the carcass middle fibers reach the yield stress limit, while the bottom fiber has a stress level higher for $\theta_{ml} = 0°$ and $180°$ and the top fiber in the opposite direction, in $\theta_{ml} = 90°$ and $270°$, with the the bottom fiber plastic hinges occurring in the angular interval of [127.75º, 52.5º] and [78.75º, 101.25º].

A set of flexible pipe structures was chosen to derive a semi-empirical equation to predict the symmetric collapse pressure of flexible pipes. The choice of thestructures was based on the number of pipes in operation worldwide, totaling 14 structures, whose nominal characteristics were combined with a set of seven ovalization o values (0.1%, 0.2%, 0.5%, 1.0%, 2.0%, 3.0%, and 4%), six values of effective stress of the carcass σ_{ef}^{c} (200 MPa, 300 MPa, 400 MPa, 500 MPa, 600 MPa and 700 MPa) and five values of pressure armor σ_{ef}^{p} (200 MPa, 400 MPa, 600 MPa, 800 MPa and 900 MPa), totaling 2940 FE analyses. The characteristics of the analyses were grouped into dimensionless parameters obtained by inspecting the FE results and previously presented analytical equations. Finally, a semi-empirical equation to estimate the collapse pressure related to the symmetric collapse mode of flexible pipes was proposed, relying on the constructed database and the software Turingbot.

Moreover, the study also showed the excellent fit of the equation in other structures not seen by the model during the training phase, which reinforces that the proposed equation can generalize and fit the problem well.

The bisymmetric and symmetric failure modes were compared using the analytical equation proposed by SOUSA *et al.* (2022) and the one obtained in this work. This comparison shows that for most of the analysis matrix cases, the symmetric collapse pressure is lower than the bisymmetric one. In the cases where the opposite is true, these pressures are close to each other, having no single isolated parameter that could

differentiate both collapse modes. When analyzing the distributions of the dimensionless parameters Π_{O_C}, Π_{σ_C} and Π_r, the threshold $\Pi_{o_C} < 3$ and $\Pi_r < 2$ seems to indicate a case of symmetric collapse pressure greater than bisymmetric collapse pressure, i.e., a case where the structure could choose the bisymmetric collapse mode instead of the symmetric one.

Future works on symmetric hydrostatic collapse analysis could focus on expanding the analysis matrix dimensionless parameter ranges, shown in Table 4-2, to investigate if there is a clear distinction between the structure failure modes (symmetric or bisymmetric), especially in the region of the identified thresholds. The influence of the gap and curvature on the collapse pressure and the associated dimensionless parameters could be explored. Additionally, the influence of increasing the polymeric layer thickness can be investigated, as it may require a different finite element model approach for large polymeric layers. Comparing the analytical equation with experimental tests is also an important area of study, which may require calibration. Finally, new dimensionless parameters inspired by those presented in this work could be proposed for symmetric hydrostatic collapse analysis, once this study took advantage of dimensionless parameters proposed on the study of bisymmetric collapse.

REFERENCES

ALEXELSSON, G. & SKJERVE, H., 2014. *Flexible Riser Carcass Collapse Analysis - Sensitivity on Radial Gaps and Bending*. Proceedings of the 33rd International Conference on Ocean, Offshore and Artic Engineering: San Francisco, California, USA.

API RP 17B, 2014. *Recommended Practice for Flexible Pipe*. 5th ed. Washington: American Petroleum Institute.

API SPEC 17J, 2014. *Specification for Unbonded Flexible Pipe*. 4th ed. Washington: American Petroleum Institute.

BAI, Y. et al., 2016. Confined Collapse of unbonded Multi-Layer Pipe Subjected to External Pressure. *Composite Structures 158*, pp. 1-10.

CHEN, C., LUO, C. & JIANG, Z., 2018. Block building programming for symbolic regression. *Neurocomputing*, Volume https://doi.org/10.1016/j.neucom.2017.10.047, p. 1973–1980.

CHEN, Y. G. et al., 2015. An Analytical Approach for Assessing the Collapse Strength of an Unbonded Flexible Pipe. *Journal of Marine Science and Application*, pp. 196-201.

CRUZ, F. T. L. & DIAS, C. A. N., 1997. *Structural Analysis of Flexible Pipe using finite element method*. Proceedings of the 7th International Offshore and Polar Engineering Conference: Honolulu, USA.

EIBEN, A. & SMITH, J., 2015. *Introduction to Evolutionary Computing*. *In Natural computing series*. 2nd ed. s.l.:Springer.

FERGESTAD, D. & LØTVEIT, S. A., 2017. *Handbook on Design and Operation of Flexible Pipes*. NTNU / 4Subsea / SINTEF Ocean: Trondheim, Norway.

GLOCK, D., 1977. *Überkritisches Verhalten eines Starr Ummantelten Kreisrohres bei Wasserdrunck von Aussen und Temperaturdehnung (Post-critical behavior of a rigidly encased circular pipe with external pressure and temperature expansion).* Der Stahlbau: .

IWANAGA, T., USHER, W. & HERMAN, J., 2022. Toward SALib 2.0: Advancing the accessibility and interpretability of global sensitivity analyses. *Socio-Environmental Systems Modeling,* Volume 4.

LI, X., JIANG, X. & HOPMAN, H., 2018. A Review on Predicting Critical Collapse Pressure of Flexible Risers for Ultra-Deep Oil and Gas Production. *Applied Ocean Research 80*, pp. 1-10.

LI, X., JIANG, X. & HOPMAN, H., 2020. Predicting the Wet Collapse Pressure for Flexible Riser with Initial Ovalization and Gap: An Analytical Solution. *Marine Structures 71*, p. 102732.

MARTINS, C. A., PESCE, C. P. & ARANHA, J. A. P., 2003. *Structural Behavior of Flexible Pipe Carcass During Launching*. Proceedings of the 20nd International Conference on Offshore Mechanics and Artic Engineering: Cancun, Mexico.

MELENDEZ, R. C., HERNÁNDEZ, O. C., HERNÁNDEZ, A. O. V. & VAZ, M. A., 2017. Finite Element and Theoretical Analyses of Bisymmetric Collapses in Flexible. *Ocean Engineering 140*, pp. 195-208.

MERINO, H. E. M., SOUSA, J. R. M., MAGLUTA, C. & ROITMAN, N., 2009. *On the Coupled Extensional-Torsional Response of Flexible Pipes.* 28th International Conference on Ocean, Offshore and Artic Engineering: Honolulu, Hawaii, USA.

MIYAZAKI, M. N. R., 2015. *Stress Analysis of a Flexible Pipe Tensile Armor Wire During and After the End-Fitting Mounting,* Dissertação M.Sc., COPPE/UFRJ: Rio de Janeiro, RJ, Brasil.

NETO, A. G. et al., 2012. *Wet And Dry Collapse of Straight And Curved Flexible Pipes: a 3D FEM Modeling*. Paper Presented at the 22nd International Offshore and Polar Engineering Conference: Rhodes, Greece.

NETO, A. G. et al., 2016. Simplified Finite Element Models to Study the Dry Collapse of Straight and Curved Flexible Pipes. *Journal of Offshore, Mechanics and Artic Engineering 138*, pp. 1-9.

PAUMIER, L., AVERBUCH, D. & FELIX-HENRY, A., 2009. *Flexible Pipe Curved Collapse Resistance Calculation*. Proceedings of the ASME 2009 28th International Conference on Ocean, Offshore and Arctic Engineering: Honolulu, Hawaii, USA.

PITTA, A. S., 2010. *Análise do Comportamento Estrutural da Armadura de Pressão de um Duto Flexível Sujeito à Carga Axissimétrica pelo Método de Elementos Finitos,* Dissertação de M.Sc., COPPE/UFRJ: Rio de Janeiro, RJ, Brasil.

PROTASIO, M. K., 2017. *Formulações Semi-Empíricas para o Colapso Hidrostático Bi-Simétrico de Dutos Flexíveis,* Dissertação de M.Sc., COPPE/UFRJ: Rio de Janeiro, RJ, Brasil.

SAEVIK, S., GRAY, L. J. & PHAN, A. V., 2001. *A Method for Calculating Residual and Transverse Stress Effects in Flexible Pipe Pressure Spirals.* In: Proceedings of the 20th International Conference on Ocean, Offshore and Artic Engineering: Rio de Janeiro, RJ, Brazil.

SILVA, J. L., 2014. *Desenvolvimento e Calibração Experimental de Modelo Numérico Baseado em Teoria de Viga para Estimativa da Pressão de Colapso de Dutos Flexíveis.* Dissertação M.Sc, COPPE/UFRJ: Rio de Janeiro, RJ, Brasil.

SOUSA, J. R. M., 2005. *Análise Local de Linhas Flexíveis pelo Método dos Elementos Finitos,* Tese D.Sc. COPPE/UFRJ: Rio de Janeiro, RJ, Brasil.

SOUSA, J. R. M., PROTASIO, M. K. & SAGRILO, L. V. S., 2018. *Equivalent Layer Approaches to Predict the Bisymmetric Hydrostatic Collapse Strength of Flexible Pipes.* 37th International Conference on Ocean, Offshore and Artic Engineering: Madrid, Spain.

SOUSA, J. R. M., SAGRILO, L. V. S. & ROCHA, D. M., 2022. *Semi-empirical equations to predict the bisymmetric dry and wet collapse strengths of flexible pipes.* Applied Ocean Research 122: s.n.

SOUZA, A. P. F., 2002. *Colapso de Dutos Flexíveis Sob Pressão Externa,* Dissertação de M.Sc, COPPE/UFRJ: Rio de Janeiro, RJ, Brasil.

TANG, M., LU, Q., YAN, J. & YUE, Q., 2016. Buckling Collapse Study for the Carcass Layer of Flexible Pipes Using a Strain Energy Equivalence Method. *Ocean Engineering 111*, pp. 209-217.

TANG, M. et al., 2015. *Residual Stress Evaluation and Buckling Analysis of Carcas Layers in Flexible Pipes Using 3D Finite Elemen Model.* Proceedings of the ASME 34th International Conference on Ocean, Offshore and Artic Engineering: St. Johns, Newfoundland, Canada.

TechnipFMC plc, 2019. *Flexible Pipes.* [Online] Available at: https://www.technipfmc.com/en/what-we-do/subsea/subsea-systems/subsea-infrastructure/flexible-pipes
[Acesso em 30 March 2021].

TIMOSHENKO, S. & GERE, J., 1961. *Theory of Elastic Stability*. 2nd ed. : McGraw-Hill.

TURINGBOT SOFTWARE CONSULTORIA EM TECNOLOGIA DA INFORMAÇÃO LTDA, 2024. *TuringBot Software.* [Online] Available at: https://turingbotsoftware.com/
[Acesso em 04 March 2024].

VAN LAARHOVEN, P. J. M. & AARTS, E. H. L., 1987. *Simulated annealing: theory and applications.*. 1st ed. s.l.:Springer eBooks.

WITZ, J. & BURKE, R. N., 1995. *Polymer Deformation in High Pressure Flexible Flow Lines,* In: Proceedings of the Seciond European Conference on Flexible Pipes Umbilicals and Marine Cables: ch. 12, London, Aug.

XAVIER, F. G., 2009. *Avaliação da vida em fadiga de um novo modelo de terminal conector para dutos flexíveis,* Tese D.Sc., PPGEM/UFRGS: Porto Alegre, RS, Brasil.

ZHANG, Y. et al., 2003. *State of the Art Analytical Tools Improve Optimazation of Unbonded Flexible Pipes for Deepwater Environments.* Proceedings of Offshore Technology Conference: Houston, Texas, USA.

APPENDIX A – Bisymmetric Wet Collapse Equations

SOUSA *et al.* (2022) defined the dimensionless wet collapse pressure $\left(\Pi_{\mathrm{p}_{cr}}\right)_W$ using Eq. (52).

$$\left(\Pi_{\mathrm{p}_{cr}}\right)_W(\overline{X}) = \frac{\Pi_{\sigma_\mathrm{C}}}{b_{1,4} + f_{W,1}(\overline{X})} + \mathrm{f}_{W,2}(\overline{X}) \tag{52}$$

where:

$$f_{W,1}(\overline{X}) = \mathrm{b}_{2,4} \cdot \Pi_{\sigma_\mathrm{C}} \cdot \Pi_{\mathrm{o_C}} \cdot \max\left[\Pi_\mathrm{r}, \mathrm{b}_{3,4}\right] - \Pi_\mathrm{r} \cdot \min\left[\mathrm{b}_{4,4} \cdot \Pi_{\sigma_\mathrm{C}}, b_{5,4}\right] \tag{53}$$

$$f_{W,1}(\overline{X}) = b_{6,4} \max\left[\Pi_{\sigma_C} \cdot \Pi_r - b_{7,4} \cdot (\Pi_r)^2, \Pi_{\sigma_C} \cdot \Pi_{o_C} logistic\left(b_{8,4} \cdot \Pi_r\right)\right] \tag{54}$$

$$logistic(x) = \frac{1}{1 + e^{-x}} \tag{55}$$

being $\overline{X_i} = \langle \Pi_{o_P}, \Pi_{\sigma_P}, \Pi_{o_C}, \Pi_{\sigma_C}, \Pi_\mathrm{r} \rangle_i$ and $b_{i,4}, i = 1$ to 8 are given in Table A-1.

Table A-1: Coefficients $b_{i,4}$

Coefficient	Value
$b_{1,4}$	9.83E-01
$b_{2,4}$	3.55E-01
$b_{3,4}$	3.17E-01
$b_{4,4}$	1.97E-01
$b_{5,4}$	2.88E-01
$b_{6,4}$	6.98E-02
$b_{7,4}$	-5.99E-02
$b_{8,4}$	7.82E-01